UNIVERSITÀ DEGLI STUDI DI PADOVA

Dipartimento di Fisica e Astronomia "Galileo Galilei"

Corso di Laurea Magistrale in Fisica

Tesi di Laurea

Fabrication and characterization of photogalvanic quantum wells

Relatore

Dr. Marco Bazzan

Correlatori

Prof. Alessandro Patelli,

Prof. Paolo Umari

Laureando

Giulio Favaro

Anno Accademico 2018/2019

Abstract

Modern photovoltaic devices based on semiconductors rely on the aid of a p-n junction to convert light into an output current. This, while enabling the production of electrical energy from the light, prevents the voltage to be greater than the material bandgap, limiting the maximum efficiency to be less than 33.16 % (Shockley-Queisser limit).
Polar crystals recently raised as an intriguing possible alternative since those materials bring a strong inversion symmetry breaking, allowing for the spontaneous separation of photo-excited carriers without the need of a space charge field localized at the junction.This could provide a way to overcome the Shockley-Queisser limit. These materials however up to now exhibit poor experimental performances whose cause is mainly attributed to the strong coupling of the carriers with the lattice that turns them into low-mobility polarons.
It is argued that a reduction of the crystal size to the nanoscale may forbid self-trapping of charge carriers due to a synergy between quantum effects and short interaction lengths, thus boosting the conversion efficiency to exploitable levels.
In this thesis we aim to start an experiment to study the photo-galvanic properties of a prototypical polar material, lithium niobate, $LiNbO_3$, when the size of the system is decreased at the nanoscale. We will lay the ground both at theoretical and experimental level to enable the fabrication of lithium niobate nano-crystalline films sandwiched between a suitable electrode geometry. In order to do so the project is articulated in three different parts: ab initio study of the photoemitted charge thermalization length, production of the samples and characterization.
The ab intio study will lead to a seizure of the photoemitted "hot" carrier energy spectrum and thermalization distance. This will provide an estimation of the critical size of the film below which the generation efficiency should display the expected enhancement. The sample production will be performed by means of rf sputtering deposition. To ensure the growth of proper film with excellent crystallinity we will use a substrate that could act both as an electrode for and as an epitaxial frame for the growth of $LiNbO_3$. Our research lead us to GaN: this material has already be proven as a viable epitaxial-ready substrate for $LiNbO_3$ while also being a semiconductor. Besides our research, investigating the fabrication and the electrical properties of such a system is therefore of great importance in view of the emerging topic of semiconductor/ferroelectric hybrid

structures.
Finally, the produced samples will be characterized by means of HRXRD, AFM, and optical absorption spectroscopy to obtain a full picture of the sample structure and composition as a function of the deposition parameters.

Contents

Chapter 1

Introduction

As the time will pass many of the scientific topics we value today will fade away and only a restricted selection will be remembered. One of the few battles that will surely survive and will come to be one of the defining characteristic of our time will be the struggle to achieve a more sustainable and environment friendly society.
One of the main setback to achieve this goal, if not the biggest one, is the impact on the planet of energy production. Traditional methods, that relies on fossil fuels, impose an high toll to the environment and so the hunt for alternatives is on.
Solar energy is the most promising renewable energy source known up to now. The high power that the sun irradiates to us could sustain an energy demand several times bigger than the current world consumption. Although potentially perfect for our objective three main obstacles impede a full conversion to this source: low conversion efficiency from radiation to electrical energy, lack of optimal methods to store and distribute the energy produced, and need to find sustainable ways to produce and recycle solar devices.
Let's focus from now on on the first of these issues. The most efficient ways to produce electrical energy from radiation up to now is represented by solar cells, the basic component of a solar panel. Three elements are required to obtain a solar cell: a process to absorb photons and convert them in excitons or electron-hole pairs, a method to separate the generated charges to prevent their recombination, and an apparatus able to collect those charges into a current.
The most widespread model of those devices it's the p-n junction solar cell that relies on a p-n junction between two different materials, characterized by majority carriers with opposite signs, to achieve charge separation. Although this scheme is currently one of the best solutions known to the problem, the cell efficiency is already reaching close to its own maximum efficiency. In fact, the Schockley - Quiesser limit predicts that the maximum output voltage that can be developed across the poles of a p-n junction cananot be larger than the bandgap energy.
In recent times a special case of photovoltaic emission is gaining more and more

interest as a possibility to overcome this limitation and achieve higher efficiencies: the anomalous photovoltaic effect. This process, observed in polar materials, consists in the spontaneous generation of a bulk current density when the crystal is illuminated with visible light. This process, radically different from the one of p-n junctions, does not require the presence of an internal space charge field and results in the buildup of large open circuit voltages several times larger than the bandgap. This phenomenon, arising in non-centrosymmetric crystals, is due to the intrinsic asymmetry of the electric potential inside the unit cell, allowing to obtain the separation of the photo induced charges. Since this particular variant of the process can be achieved by large single crystals it is usually referred as the Bulk photogalvanic effect (BPGE).
Theoretically, the BPGE may allow for higher conversion efficiencies than the ones predicted by Shockley and Queisser. Unfortunately, the short-circuit current of these materials is generally low, so that presently they cannot be used in practical power-generation systems.
However, a few recent works on this topic report that the photogalvanic current displays an exceptional enhancement in nano-materials. If the current increase could be mastered and engineered, new and highly efficient photogalvanic cells could be developed. Interestingly, this appears to be a general phenomenon, independent on the specific choice of the polar crystal. Up to now, however, no coherent explanation for this effect has been provided yet. Objective of this thesis is to study the possibility to create nanofilms of a prototypical BPGE crystal, lithium niobate, devising a procedure to be used to grow and characterize nanofilms for further studies. The sought films need to be of high crystalline quality, with the possibility to finely tune their thickness at the nanometer level. Moreover they need to electrically contacted with electrode materials on their polar faces to enalble photocurrent measurements. In the following we will detail the research on this topic. *Ab initio* simulations of the system will be used to get an estimate of the characteristic thermalization lenght of "hot" photoemitted electrons, which will set the thickness scale of the film to be realized. Next, the experimental procedure to produce high- quality $LiNbO_3$ ultra -thin films by the mean of the sputtering technique will be studied. Finally the produced samples will be characterized by HRXRD, AFM and optical absorption spectroscopy.

Chapter 2

State of the Art

2.1 Solar cells

A solar or photovoltaic cell is a device able to harness energy from photons, usually only in the visible range, and converting them into electricity by the mean of the photovoltaic effect. the principle on which a solar cell works is very similar to a photo detector differentiating mainly by the output power it can sustain.
In a common solar cell three steps must happen to convert radiation into electrical energy: the incoming photons must be absorbed and converted in a charged carrier either by generating an electron-hole pair or an excitons such as a polaron. The photo charges generated tend to simply recombine themselves into the ground state configuration; to prevent this from happening a mechanism that separates the charges must take place. Charges must then be extracted from the material and forced into an external circuit to make the process useful.
A common type of such a device is a p-n junction. In such a configuration

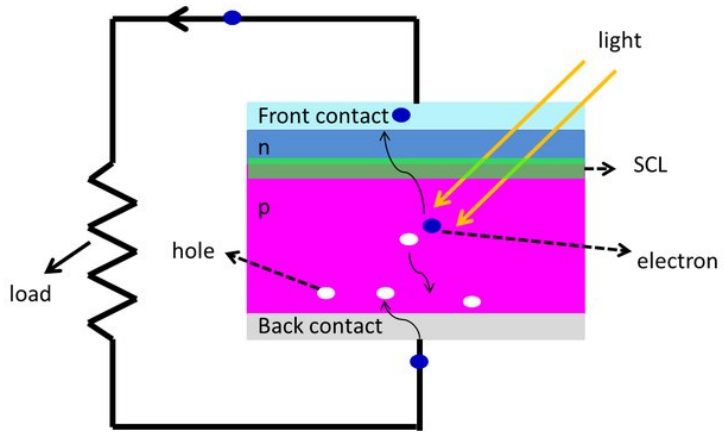

Figure 2.1: p-n junction solar cell

an incoming photon excite an electron from the valence level and raise it to the conduction band: the electrical field present inside the material because of the depleting region of the junction force the electron and the hole generated to move into opposite directions. By placing two electrodes on the two opposing surfaces of the material the charges can be made move through a load effectively generating power.
Efficiency of single p-n junction solar cell can be calculated following a very general approach on the main loss factor of such a system as done by Shockley and Queisser in 1961. The core role in Shockley and Queisser reasoning is played by the bandgap of the material used in the junction. Since the photoexcitations take place from the valence to the conduction state the minimum energy required to the photon to start the process is equal to the bandgap thus the smaller the bandgap the higher the percentage of light spectra we are able to use. A small bandgap however damage the efficiency of the device too: electrons that travels through the material loose energy and place themselves on the bottom of the conduction band. In such a state their probability of spontaneous recombination is greater for smaller values of the gap and also the maximum power they are able to generate is smaller being placed at a smaller voltage.
This limit predict for a single p-n junction a maximum efficiency of 33.7 % at 1.34 eV [50]; a possible way to increase the efficiency of the process would be if it was possible to obtain an open circuit voltage higher than the bandgap. Turns out that a particular kind of photovoltaic emission called anomalous photovoltaic effect or, for single crystals, bulk photogalvanic effect satisfy this condition with the term anomalous pointing exactly to the unusual voltage it can sustain.
There are three possible systems that are known to exhibit this effect: polycrystalline materials, ferroelectrics with multiple domains and non centro-symmetric single crystals [2]. For the first case the single grains of the material can act as a stack of cells adding their total voltage. In a similar fashion for certain ferroelectrics with multiple domains the single domains can act in the same way establishing an high voltage perpendicularly to the ferroelctric orientation. The last case occurs when due to the non centro-symmetry of a crystal, and such typical of polar crystals, the charge creation and/or the charge transport processes have non symmetric distributions [3].
In this latter case the photovoltages are exceptionally high and not directly tied with the bandgap: due to intrinsic asymmetry of the potential each time a photon gets absorbed statistically a charge shift happens inside the crystal usually of a few unit cells. This mechanism however also points out the main issue of this effect: its low efficiency: since the net effect of a single photon is just a tiny displacement many photons are needed to extract even a single charge.
A possible solution could be to reduce the crystal that exhibit this effect from a bulk to a thin film with a dimension comparable with the length the charge carrier travel before stopping again to diminish the number of photoexcitations needed.

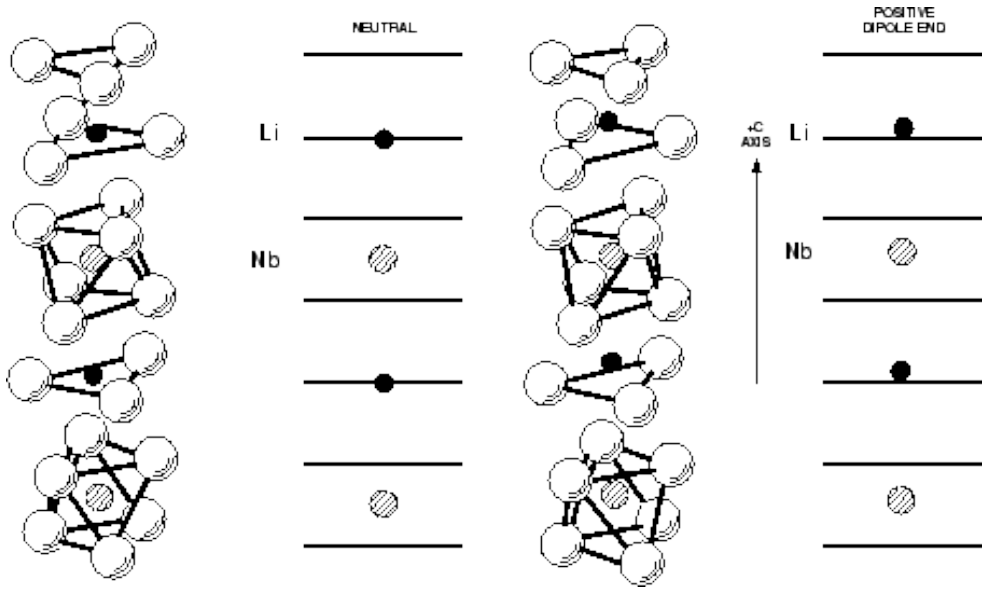

Figure 2.2: Paraelectric and ferroelectric atoms dispositions in lithium niobate

2.2 lithium niobate

There are several material known to exhibit the Bulk photogalvanic effect, among them we chose to focus our efforts on lithium niobate as this material is a prototypical case, it is readily available in high quality at a reasonable price and is a widely studied, well known ferroelectric material. Moreover, it has already been demonstrated in literature that this material can be sinthesized in the form of highly oriented thin crystalline films, and so is an ideal candidate for our research.

Lithium niobate is a synthetic material, not present in nature, described for the first time in 1928 by Zachariaesen, discovered ferroelectric in 1949 by Matthias e Rameika [13] and firstly studied at Bell laboratories in 1966 [8] [9] [10] [11] [12]. $LiNbO_3$ is a dielectric and ferroelectric material widely known for its electro-optic applications and acousto-optic ones due to various kinds of pronounced physical properties.

$LiNbO_3$ belongs with $LiTaO_3$ and $BaTiO_3$ to the ABO_3 type ferroelectrics. Ferroelectricity of lithium niobate like many other of its physical properties can be understood by its crystal lattice structure so we will now look into it. In Figure 2.2 a basic representation of $LiNbO_3$ atoms disposition for both the ferroelectric and the paraelectric phase is depicted. Lithium niobate lattice structure is composed by oxygen planes disposed in a closed-packed configuration. The octahedra formed by the oxygens are the interstitial spaces to be filled by niobium and lithium atoms in the structure. In the ideal stoichiometric composition, those sites are for one third filled with Nb, for one third filled with Li, and the rest remain empty: along the axis perpendicular to the oxygen planes the octahedra filling sequence is Li-Nb-V.

This direction defines the polar axis of the crystal, commonly referred as $\hat{c}$ or z,

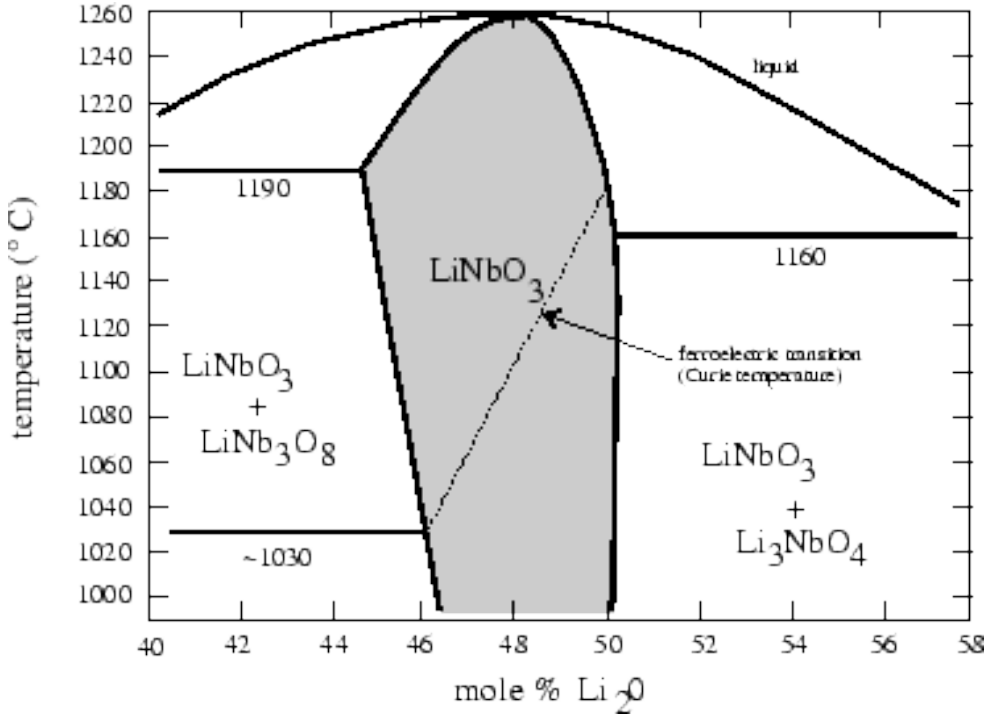

Figure 2.3: Caption

that is also the optical axis. Reason for this behaviour can be found in the positions of Li and Nb atoms: in the paraelectric configuration of the crystal they assume a symmetric position in the lattice with the niobium atoms placed in between two oxygen planes and the lithium ones aligned with one of the planes; in the ferroelectric phase however Li and Nb atoms displace themselves along the $\hat{c}$ axis, breaking the centro-symmetry of the elementary cell and creating an elementary dipole for the material.
Chemical synthesis of lithium niobate happens with the reaction

$$\mathrm{Li_2CO_3} + \mathrm{Nb_2O_5} \rightarrow 2\,\mathrm{LiNbO_3} + \mathrm{CO_2} \tag{2.1}$$

and its usually grown into single crystals by the Czochralski technique. In **??** the phase diagram of $LiNbO_3$ is depicted. One of the main features of lithium niobate is to have an ample region of existence respect the percentage of $Li_2\,O$ in the material; for a value of 48.45 % mol the system is said to be congruent and the liquid and the solid phase have the same composition. As a consequence of this fact, stoichiometric $LiNbO_3$ it's hard to grow to the point that only this Li deficient version of the crystal, called congruent, is available in commerce. Many physical properties of lithium niobate are strongly dependent on the molar composition; this led to a better characterization of congruent respect to stoichiometric lithium niobate to the point that the former is the standard one used in any application.
The Curie temperature of $LiNbO_3$, although dependent on composition, is quite high in particular with respect to its fusion temperature of 1257 °C averaging at

1142 °C so at room temperature the material is in its ferroelectric phase.
Lithium niobate lattice, since exhibit a three-fold rotation symmetry around its $\hat{c}$ axis, belongs to the trigonal crystal system with *R3c* space group and point group *3m* while below Curie temperature, and *R3m* when above it, restoring its centro-symmetry.
In trigonal systems two different unit cells can be used: hexagonal and rhombohedral, however its far more common to express all tensorial properties within a Cartesian frame. The z axis is chosen perpendicular to the oxygen planes and parallel to the $\hat{c}$ axis. For the y axis, one of the mirror planes is taken as reference and this axis lays on it, and lastly the x axis is simply defined perpendicular to the previous two ones. The axis are oriented such as both z and y, when an uniaxial compression is applied along them, see a negative charge appearance on their positive end (piezoelectricity). Commercially available lithium niobate crystals usually come as wafer cut along a specific orientation.
Most of the properties that characterize lithium niobate descend directly from the intrinsic displacement that Nb and Li atoms exhibit from the paraelectric phase and their changes induced by either a change in temperature or pression. $LiNbO_3$, being a ferroelectric, presents a spontaneous polarization at room temperature $|\vec{P}| = 0.21\,\mathrm{C/m^2}$: an applied stress or a temperature change affect the spontaneous polarization so that the material is piezoelectric and pyroelectric [16]. These two properties can be easily described in a tensorial formalism: for pyroelctricity we have

$$\Delta P_i = p_i \Delta T$$

Pyroelectric coefficients in $\mathrm{C/m^2K}$

p_1	p_2	p_3	Ref.
0	0	-4×10^{-5}	[22]

For piezoelctricity we will need a rank three tensor, d_{ijk}, to be coupled with the stress tensor σ_{jk}. Stress tensor can be shown in general to be a rank two symmetric tensor conversely any physical property related to it must obey the same relation. Applying this idea we can define a new subscription for jk transforming rank three tensors into 3x6 matrices with the Voigt rules [26]:

$$\begin{array}{ll} 11 = 1 & 23{,}32 = 4 \\ 22 = 2 & 31{,}13 = 5 \\ 33 = 3 & 12{,}21 = 6 \end{array}$$

Piezoelectric relation so can be written as:

$$\Delta P_i = \sum_{jk} d_{ijk} \sigma jk$$

Piezoelctric strain coefficients in $10^{-11}\,\mathrm{C\,N^{-1}}$

d_{15}	d_{22}	d_{31}	d_{33}	Ref.
6.92	2.08	-0.085	0.60	[34]
6.8	2.1	-0.1	0.6	[33]
7.4	2.1	-0.087	1.6	[35]

where d_{ijk} has the form:

$$d_{ijk} = \begin{bmatrix} 0 & 0 & 0 & 0 & d_{15} & -2d_{22} \\ -d_{22} & d_{22} & 0 & d_{15} & 0 & 0 \\ d_{31} & d_{31} & d_{33} & 0 & 0 & 0 \end{bmatrix} \tag{2.2}$$

As we can see only few components of this tensor are independent one from each other. This is a consequence of the intrinsic symmetries of the crystal lattice. Lithium niobate crystal belongs to the *3m* point group so conversely any tensor describing properties of the crystal must satisfy at least the same symmetries. Directly tied with a crystal composition and symmetries there are the elastic properties. They can be described by the resulting strain originating from an applied stress and, when under the limit for a plastic deformation, the relation can safely be assumed to be linear following the Hooke's law and so the components of the stress can be written as:

$$S_{ij} = \sum_{k,l} c_{ijkl}\sigma_{kl} \tag{2.3}$$

where σ_{kl} describe the stress on the material. An inverse relation can be written as well:

$$\sigma_{ij} = \sum_{k,l} s_{ijkl}S_{kl}. \tag{2.4}$$

These two tensors s_{ijkl}, called elastic stiffness, and c_{ijkl}, called compliance, by reducing both the stress and the strain tensors with the same subscription as before, can be written as 6x6 matices:

$$s_{ij} = \begin{bmatrix} s_{11} & s_{12} & s_{13} & s_{14} & 0 & 0 \\ s_{12} & s_{11} & s_{13} & -s_{14} & 0 & 0 \\ s_{13} & s_{13} & s_{33} & 0 & 0 & 0 \\ s_{14} & -s_{14} & 0 & s_{44} & 0 & 0 \\ 0 & 0 & 0 & 0 & s_{44} & 2s_{14} \\ 0 & 0 & 0 & 0 & 2s_{14} & 2(s_{11} - s_{12}) \end{bmatrix} \tag{2.5}$$

$$c_{ij} = \begin{bmatrix} c_{11} & c_{12} & c_{13} & c_{14} & 0 & 0 \\ c_{12} & c_{11} & c_{13} & -c_{14} & 0 & 0 \\ c_{13} & c_{13} & c_{33} & 0 & 0 & 0 \\ c_{14} & -c_{14} & 0 & c_{44} & 0 & 0 \\ 0 & 0 & 0 & 0 & c_{44} & 2c_{14} \\ 0 & 0 & 0 & 0 & 2c_{14} & 2(c_{11} - c_{12}) \end{bmatrix} \tag{2.6}$$

s_{11}	s_{12}	s_{13}	s_{14}	s_{33}	s_{44}	Ref.
5.831	-1.150	-1.452	-1.000	5.026	17.10	[34]
5.78	-1.01	-1.47	-1.02	5.02	17.0	[33]
5.64	-	-	-0.84	4.94	-	[35]

Table 2.1: Elastic compliance coefficients at constant electric field in $10^{-12}\,\mathrm{m}^2/\mathrm{N}$

c_{11}	c_{12}	c_{13}	c_{14}	c_{33}	c_{44}	Ref.
2.030	0.573	0.752	0.085	2.424	0.595	[34]
2.03	0.53	0.75	0.09	2.45	0.6	[33]

Table 2.2: Elastic stiffness coefficients at constant electric field in $10^{11}\,\mathrm{N/m^2}$

The main properties of $LiNbO_3$ that led to such an intense study on this material are its optical properties. Lithium niobate is a transparent medium with a negligible absorption index in the 0.35-3.5 µm that a shows an high sensitivity from defects and impurities in the lattice [24] fact that will be exploited in chapter 5. It possesses a large natural birefringence: this means that the permittivity of the material is expressed by an anisotropic tensor

$$\epsilon = \begin{bmatrix} \epsilon_{11} & 0 & 0 \\ 0 & \epsilon_{11} & 0 \\ 0 & 0 & \epsilon_{33} \end{bmatrix}$$

Relative permittivity coefficients

ϵ_{11}	ϵ_{33}	Ref.
0	0	[33]
0	0	[34]
0	0	[35]

and that we can define two refractive indexes: $n_o = \sqrt{\epsilon_{11}/\epsilon_0}$ and $n_e = \sqrt{\epsilon_{33}/\epsilon_0}$ the former called 'ordinary' applies to waves polarized perpendicularly to the optical axis (z-axis) of the crystal while the latter applies to waves polarized in a parallel way.
The application of an electric field affects the spontaneous polarization of the material due to the coupling with the positions of Li and the Nb present inside the lattice leading to one of the key properties of lithium niobate that rendered it, in the years, a leading material for optical applications: the linear electro-optic effect. Materials that possess the linear electro-optic effect show a linear response on the impermeability tensor $\left(\frac{1}{n^2}\right)_{i,j}$ when an electric field is applied. This relation can be written as:

$$\Delta\left(\frac{1}{n^2}\right)_{i,j} = \sum_k r_{ijk} E_k$$

Linear electro-optic coefficients in $10^{-12}\,\mathrm{m\,V^{-1}}$

r_{13}	r_{22}	r_{33}	r_{42}	Ref.
28	3.4	8.6	30.8	[36]
23	3.1	6.5	28	[37]

where r_{ijk} in Voigt notation assumes the form:

$$r_{ijk} = \begin{bmatrix} 0 & -r_{22} & r_{13} \\ 0 & r_{22} & r_{13} \\ 0 & 0 & r_{33} \\ 0 & r_{42} & 0 \\ r_{42} & 0 & 0 \\ -r_{22} & 0 & 0 \end{bmatrix} \tag{2.7}$$

From the point of view of light photoexcitation, when lithium niobate is subjected to visible or UV illumination, some charges may be photoexcited either from donor levels located in the bandgap, either by intrinsic interband transitions. This gives rise to two effects: photoconductivity and bulk photogalvanic effect. The interplay with those two phenomena may lead to the formation of intense space charge fields inside the illuminated areas of the material. As LN is electro-optic, those fields are mapped into a refractive index modification which in turn may affect the propagation of light itself. This is the basis of the so-called photorefractive effect, enabling peculiar types of nonlinear optical phenomena even at low light intensities. This effect, firstly observed by Ashkin et al [25], is a peculiar characteristic that can be observed when the crystal is illuminated in an inhomogeneous way. In such a configuration a change in the refractive index of the material is observed and its commonly explained as a charge migration followed by an electro-optic effect. The peculiar aspect of lithium niobate is that, While there are multiple ways to build up a non uniform charge distribution in the material, the charge redistrbution under illumination is triggered by the onset of a current density in the bulk of the material, even without any physical interface inducing the charge separation. This is the essence of the bulk photogalvanic effect which will be described in detail in the next paragraphs.
We can not stress enough how important are the composition and the presence of impurities in lithium niobate in determining its physical properties. Extrinsic defects also play an important role when explaining this kind of responses. As we said $LiNbO_3$ in the congruent composition naturally comes with a Li deficiency so it naturally present itself with a defect structure embedded in the lattice to compensate the charge imbalance. We will call it the intrinsic defect structure. The most common assumption in oxide is the presence of oxygen vacancies in the lattice so the correspondent defect model is:

$$\langle LiNbO_3 \rangle \rightarrow 2\,{V_{Li}}^{-} + {V_O}^{2+} + Li_2O \tag{2.8}$$

however lithium niobate places in a particular position of having the V_O defects almost not present under normal conditions, a fact that has been shown both as an *ab initio* result [45] and proved experimentally [44].
When the presence of Li decrease, a correspondent increase on the crystal density can be observed. This is generally taken as a prove that a lithium deficiency is associated to the formation of substitutional defects Nb_{Li} [46]. The hypothesis is reasonable due to the higher mass of the niobium atom, its smaller covalent radius, and the fact that oxygen octahedra for the Li are wider than the ones for Nb. Two models have been proposed along this hypothesis: the niobium antisites model

$$\langle LiNbO_3 \rangle \rightarrow 4\,{V_{Li}}^{-} + {Nb_{Li}}^{4+} + 3\,Li_2O \tag{2.9}$$

and the niobium vacancy model

$$\langle LiNbO_3 \rangle \rightarrow 4\,{V_{Nb}}^{5+} + 5\,{Nb_{Li}}^{4+} + 3\,Li_2O. \tag{2.10}$$

Niobium antisites model presents as the most energetically favourable of these models [48] and its commonly assumed to be the mechanism explaining the

intrinsic defect structure of lithium niobate however, as some authors point out [47], the defects present in the $LiNbO_3$ crystals are far more related to the conditions of the growth process and so all 3 types of defects can be found even in the same sample.
The high concentrations of natural occurring vacancies makes the doping process of lithium niobate extremely easy and can be performed by direct melt - doping or locally with standard techniques as ion implantation. Common dopants for $LiNbO_3$ are Mg, Fe, Zr, Zn, and Hf mostly used to control the photorefractive or the photogalvanic effect. The presence of defects in the lattice, both intrinsic and extrinsic, is actually the core mechanism of these two effect because the deformed lattice structure lead to the creation of donor and acceptor levels inside the bandgap as we will see more in the detail in the next section.

2.3 Photogalvanic effect in lithium niobate: polaron model

Bulk photogalvanic effect was first discovered in lithium niobate by Glass et al. in 1974 [6] that noted how illuminating a single crystal lead to the appearance of a steady short-circuit current, proportional to intensity of the light and absorption coefficient, along the same direction of the c-axis.
The photogalvanic effect is described by a rank three tensor β_{ikl}:

$$j_{PG} = \beta_{ikl} E_k^* E_l \tag{2.11}$$

where E represent the complex amplitude of the incident electric field [52]. As before for the other tensorial properties, symmetries of the lattice limit the amount of independent components to only four: β_{zzz}, $\beta_{xxx} = \beta_{yyy}$, $\beta_{yyy} = -\beta_{xxy} = -\beta_{zz} = -\beta_{zz}$, and $\beta_{yyy} = -\beta_{xxy} = -\beta_{xyx} = -\beta_{yxx}$. It's interesting to study the behaviour of this effect in a 1D model since the current happen mainly on one direction: let's consider a light ray polarized along y then $j_x = j_y = 0$ and $j_z = \beta_{zyy} E_y^* E_y$ then it is well described by Glass phenomenological formula

$$j_{PG} = K_G \alpha I \tag{2.12}$$

where K_G is the Glass coefficient and α is the optical absorption of the material. The effect can be reduced to other experimental quantities too:

$$j_{PG} = \frac{q\alpha I}{h\nu} \Phi L_{PG} = qsN \frac{I}{h\nu} \Phi L_{PG} \tag{2.13}$$

where q is the charge of the photocarriers, $sN = \alpha$ is the absorption coefficients of the sources of the phenomenon with s their cross section, I the light intensity, Φ a correction for photorefractive effect and $h\nu$ the photon energy. The last term that shows up is of fundamental importance: it's called photogalvanic length and characterize the mean displacement of the charges caused by a single photon.

Another fundamental length we can define is the thermalization length of the process λ_t that is the mean distance travelled by a photogenerated carrier before stopping again inside the material.
A microscopic interpretation of $LiNbO_3$ bulk photogalvanic model was proposed by Schirmer et al. [51] involving the polaron states inside lithium niobate crystal as a source for the effect. The authors propose that the charge carriers in the photogalvanic effect are electron that, thanks to the photon they absorb, free themselves from a polaron state.
Defects structures cause the appearance of new energy levels even inside the bulk bandgap. For Fe_{Li} and Nb_{Li} these levels manifest as polaron states: bound states between an electron and a lattice phonon [53] [54]. Polaron states at a Fe^{2+} defect create two possible levels inside the bandgap one at 1.6 eV above the valence band with spin down, and one at 0.6 eV above the valence band with sin up. Due to the large value of the bandgap in lithium niobate only the former states can produce a photocharge by absorbing a VIS wavelength and so from now on we will refer only to this state.
In photogalvanic effect the photon absorbed is believed to interact with a bound polaron, an autolocalized polaron, at the Fe defect. This interaction frees an electron that starts moving inside the lattice: the nearest charges it sees are the eight nearest neighbour Nb^{5+} that surrounds the Fe^{2+} as in Figure 3.2 so it starts moving towards them. The electron starts its motion with a defined direction among the eight possible but moving through the lattice undergoes numerous scattering processes with the phonons loosing momenta. The thermalization length λ_t characterize the distance the electron is able to travel before being slowed enough to be captured again in a bound state.
In the accepted model when electrons loose their energy form again a polaronic state, in particular it is believed that, due to their abundance, Nb_{Li} antisites are responsible for this capture into a free polaron. This state is characterized by a low mobility so the charge diffuse slowly in the crystal until it gets captured again localizing itself on a Fe^{3+} allowing the process to start again.
As we said emission probability isn't equal among the eight direction so the net effect of this process can be thought as a mean displacement of the charges in the lattice. This quantity is the photogalvanic length L_{PG} we defined before and can be defined as

$$L_{PG} = \frac{\sum_{i=1,2,3,7} p_i(\hbar\omega)\lambda_{t_i} - \sum_{i=4,5,6,8} p_i(\hbar\omega)\lambda_{t_i}}{\sum_i p_i(\hbar\omega)} \tag{2.14}$$

where p_i are the transition probabilities.

2.4 Lithium Niobate thin films

Lithium niobate, being a ferroelectrics material, could have access to a wide range of application utilizing its peculiar properties like nonvolatile memory,

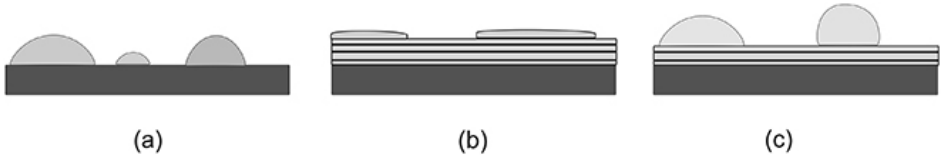

Figure 2.4: Growth models for lithium niobate

electro-optical components or acoustics devices that could greatly benefit from the reduction in dimension of the crystal in a similar way to the bulk photogalvanic effect. For this reason production of $LiNbO_3$ thin films and their characterization are hot topics in this material research.
Since as we said lithium niobate properties are highly dependent on its composition and impurities, choosing a specific deposition methods require to deeply inquire the final quality of the samples. Among the various methods used to create thin $LiNbO_3$ film we can mention Pulsed Laser Deposition, Liquid Phase Epitaxy, and Radio-Frequency Magnetron Sputtering to be among the best.
There is up to today no clear winner between all the possible method for thin films deposition since each one of them comes with its own sets of advantages and disadvantages. Pulsed Laser Deposition for example grants one of the highest degree of precision on the composition but affects only a small area and thus leads to non uniform samples [27].
In this work we will focus onto Radio Frequency Magnetron sputtering. Being adapt to deposit a wide set of materials, independently of their melting temperature, it can be used to deposit lithium niobate with the possiblity to control in several ways the final result. Moreover, high deposit rate even on large samples are possible, and by playing with the target composition, it is possible to obtain doped films. The main drawback of this technique comes from the high behavioural complexity introduced by the presence of the plasma that require a fine study of the deposition parameters.
A more in depth explanation of the sputtering process will be given in chapter 5 but basically it consist on the erosion of a target material by the mean of a plasma, usually achieved with noble gases, and the subsequent deposition of the eroded material onto a substrate.

In Figure 2.4 a representation of three commonly assumed models of the epitaxial growth are depicted [28]. The first model (a) is called the Volmer-Weber model and is most common for a low adhesion between the crystals and the substrates; in this model atoms cluster together on the surface forming island that, for long enough growth, form an united film. In (b), Frank and van der Merwe mechanism, the high adherence lead from the start to the growth a layered structure while (c), Stranski - Krastanov model, present itself as an intermediate case between the previous two models; as many authors suggest the preferred model for $LiNbO_3$ can be assumed the first one [29].
As we said, the process parameters of the sputtering deposition are extremely important to control the quality of the material obtained, the most critical ones being the substrate temperature, the atmosphere composition, the total pressure

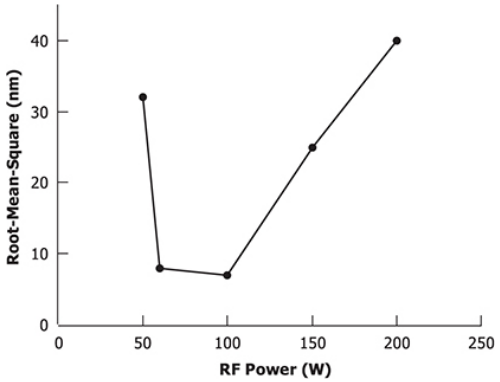

(a) RF Power study

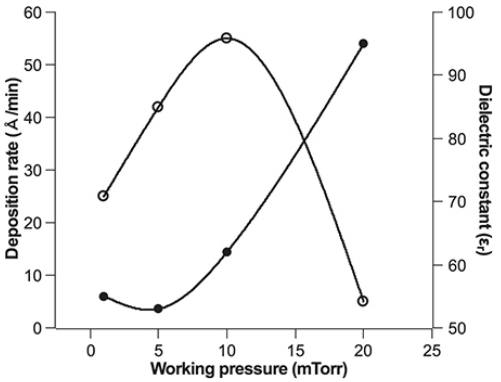

(b) Total pressure Study

inside the chamber, the composition of the target, the substate - source distance aand the RF-power used in the process.
The main defects that RF-sputtering lithium niobate films show are a deficiency in lithium, placing them on the sub-congruent side, as well as a rather high probability in growing other phases. Different quality targets have been studied in literature both sintered ones and single crystals; sintered targets allow for a more precise control of eventual dopant agents in the film and K_2O enriched targets have been shown to positively impact the quality of the film. Nevertheless, single crystal at the moment appears to be still the best solution from the point of view of the composition of the deposited films.

Concerning the RF power to be used, the main observations indicate that below 70 W only amorphous growth is reported, which can be explained by an insufficient energy of the sputtered species to perform a nucleation process. 100 W seems to be the value that minimize surface roughness of the deposited films [30]. At 100 W it is reported also that the obtained permittivity is the one most resembling the one of a bulk [31]. For higher values of the used power an increase in the cristal quality is reported, however at expensesof a faster target consumption and an higher risk of breaking it [32].
As for total working pressure, authors [40] [41] report that lower pressures (around 10 mTorr) lead to the best results from the point of view of obtaining a resemblance to bulk properties. However this comes at the price of slower depositions rates. Probably the most critical parameter is the atmosphere composition inside the chamber. It is reported [40] [30] that atmosphere composition directly affects the percentage of Li in the films and many studies have been done on this subject. O_2 was found to be linked with an increase in the partial pressure of Li in the chamber leading to near stoichiometric films however a pure oxygen atmosphere was found not able to grow crystal films [43]. Among the various studies that confronted the issues pretty much each one end with its own advice on the Ar/O_2 ratio starting to 1:1 to 5:1 with many values in between.
The reason why partial and total pressure affect the sample composition is commonly attributed to the different mass of Li and Nb: being the former far lighter is much more prone to scattering with the gases atoms inside the chamber lower-

ing the amount that reach the sample surface. For the same reason distance plays a fundamental role in the process and so the most common one used in literature, 5 cm, was used. Provided that an appropriate substrate is used, the sputtering technique can be also allow for the production of heteroepitaxial layers. In this case the substrate temperature is another critical issue. To crystallize in a high quality film one should expect that an high temperature is needed to allow ions to perform an annealing process on the surface; it has been shown that temperatures higher than 400 °C are needed to prevent amorphous films but there is also some evidence that over 650 °C dissociation of the Li might take place [42].

Chapter 3

Ab initio simulation of electron thermalization length

As already explained the absorption of a photon by a Fe defect in $LiNbO_3$ frees an electron from a polaronic state that acts as the source of the bulk photogalvanic current. The said electron maintain a certain degree of coherence while traveling in the material for a thermal length λ_t before getting transformed back into a polaron and starting a diffusion process.
This length, while extremely important to quantify the finite size effect of the crystal on the BPGE efficiency, is not experimentally known and make impossible to predict a target thickness to aim for in the production of our samples.
To overcome this obstacle we performed an *ab initio* simulation of a $LiNbO_3$ crystal bulk to extract its main physical properties and perform an estimation of λ_t.

3.1 Kohn-Sham equations and computational DFT

The Shrödinger equation for a many body system has no simple solution already for N > 2: determining the properties of a large quantum system, in our case a crystal, require so to use some degree of approximation, e.g. neglecting the interaction among electrons. Another possibility is to incorporate it by resorting to some kind of variational approach, as it will be done in the DFT method.
For solving crystal systems one usually start by accepting the Born-Oppenheimer approximation for which electrons in a crystal see the nuclei standing still allowing to decouple the equation of motion of electrons and nuclei. It is now possible, as demonstrated by Kohn and Sham, to relate the ground state properties of our system to the spatial density of electrons in a biunivocal way.
We start by decomposing the energy of the system $\hat{H}$ into the sum of three components: the kinetic energy $\hat{T}$, the potential interaction of the ionic lattice

$\hat{V}$, and the mutual interaction $\hat{U}$ of the electrons.

$$E =< \Psi|\hat{H}|\Psi >=< \Psi|\hat{T} + \hat{V} + \hat{U}|\Psi > \tag{3.1}$$

Now since the mutual interaction must depend only on the electron density we can write

$$E =< \Psi|\hat{T} + \hat{V}|\Psi > + \int U(\boldsymbol{r})\rho(\boldsymbol{r})d^3\boldsymbol{r}. \tag{3.2}$$

The Hoemberg-Kohn theorem now states that it exist a one to one correspondence between U and the internal energy $F = T + V$. Thus, there must exist a functional of the electron density that allows us to calculate the energies of our system.
One can now rewrite the many body problem as a fictitious one electron Shrödinger equation bound to generate the same charge density of the full problem by minimizing the energy functional. The most common functional used is the Kohn-Sham energy functional producing the Kohn-Sham equations:

$$\left[-\frac{\hbar^2}{2m}\nabla^2 + \hat{U}(\boldsymbol{r}) + \int d^3\boldsymbol{r'}V(\boldsymbol{r}-\boldsymbol{r'})\rho(\boldsymbol{r'}) + \frac{\delta E_{XC}[\rho(\boldsymbol{r})]}{\delta\rho(\boldsymbol{r})})\right]\phi_i(\rho(\boldsymbol{r})) = \epsilon_i\phi_i(\rho(\boldsymbol{r})) \tag{3.3}$$

where we use a Coulomb interaction in place of $V(\boldsymbol{r}-\boldsymbol{r'})$ and where $E_{XC}[\rho(\boldsymbol{r})]$ rapresent a correction to the energy of the system due to the particles being all identical. This set of equations, once solved, would allow for computing the electron density of the system and so the physical properties of the crystal. However to do so we first need the electron density making it a circular problem. What it is usually done in practice is to search for a self-consistent solution for ρ by iterating multiple times the calculation until a prefixed level of tolerance is reached.

3.2 Lithium niobate bulk simulation

The first step we need to perform in order to reach an estimate of λ_t is to prepare an environment able to reproduce the known crystal properties of lithium niobate. We will perform such a task via Quantum Espresso an integrated suite of Open-Source computer codes for electronic-structure calculations and materials modeling based on DFT, plane waves, and pseudo-potentials [7].
The procedure to determine the crystal system is as follows: first we started by assuming an initial guess value for the electron density and letting the ionic system to relax to its equilibrium position. The self-consistent electron density was then recalculated and used to derive the force acting on the nuclei. The nuclei position is then re-optimized and the cycle starts again. The procedure was repeated until the sum of the forces acting on each ionic nucleus is compatible with zero.

	Simulation result	literature values	
lattice parameter	5.514×10^{-10} m	5.151×10^{-10} m [38]	5.086×10^{-10} m [39]
$\epsilon_{\parallel}$	5.38	5.6 [38]	6.1 [39]
$\epsilon_{\perp}$	5.06	5.5 [38]	6.1 [39]
Bandgap	3.44 eV		

Table 3.1: Calculated and literature values for various physical properties

Once the computation is completed, it is possible to use the different tools of the Quantum Espresso suite to calculate a number of different physical properties of the material. By comparing them to experimentally available data one can assess the overall accuracy of the ab initio procedure. In **??** a comparison between calculated phonon values and literature ones is reported while in Table 3.1 the same was done for various other physical properties. **As it can be seen the agreement... da finire** The bandgap estimate, while being very close to the experimental values, represents a puzzle of the simulation because typical DFT computations generally tend to underestimate it. A tentative explanation of this surprisingly good accordance may be due to two errors that cancel each other: a known issue of DFT simulations is their difficulty in modelling ferroelectric materials so there is the possibility that as a fortuitous case the polar properties of lithium niobate lead to an increase in the estimate of of the bandgap resulting in a value almost equal to the experimental one. However this is just an hypothesis which would need further verification. Nevertheless, in view of the overall good agreement between the numerical and the experimental data, we can consider the results of the simulation as reliable and move to the next step.
Once the self-consistent calculation has been completed, the electronic system properties are now at hand. in particular we have access to the band structure of lithium niobate, shown in Fig. Figure 3.1 . We used this resource to compute the behaviour of an electronic charge photo-excited by a photon. As it is reported in chapter 2, in Fe- doped LN, some electronic charges are trapped at Fe impurities. When a photon with wavelength in the visible range excites the Fe impurity, the electronic charge is promoted to a state in the valence band, according to the energy of the photon energy. The results of this calculation are shown in Figure 3.1 alongside the associated density of states and a color bar showing the optical wavelength needed to excite an electron from the Fe bound state to the correspondent energy level.

3.3 Estimate of electron thermalization length

Let's do a quick recap on how the photogalvanic process happens in Fe:$LiNbO_3$. A light photon, while traveling in the material, gets absorbed by a Fe_{Li} defect,

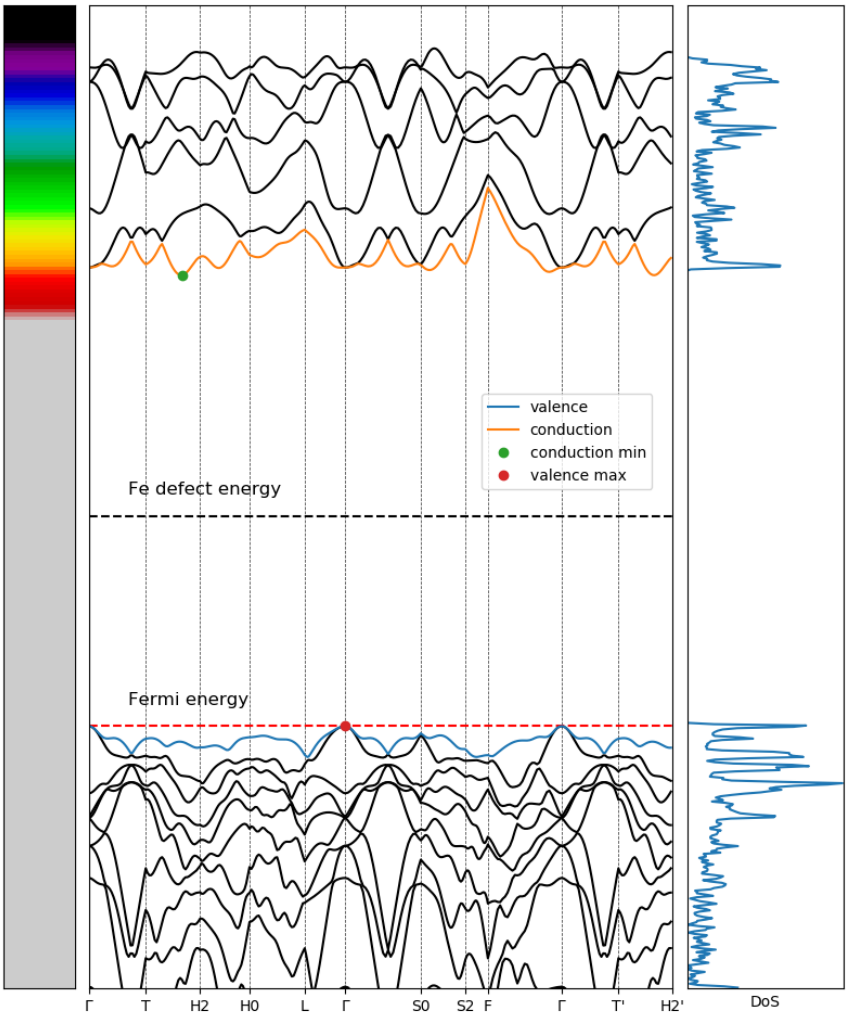

Figure 3.1: Calculated Band structure and DoS for $LiNbO_3$. The color bar on the left represent the energy of the photon required to excite an electron from the Fe defect to the correspondent energy level. The Fermi energy refers to a non doped lithium niobate crystal while the black line represent the energy of a polaron bounded on a spin down Fe^{2+}

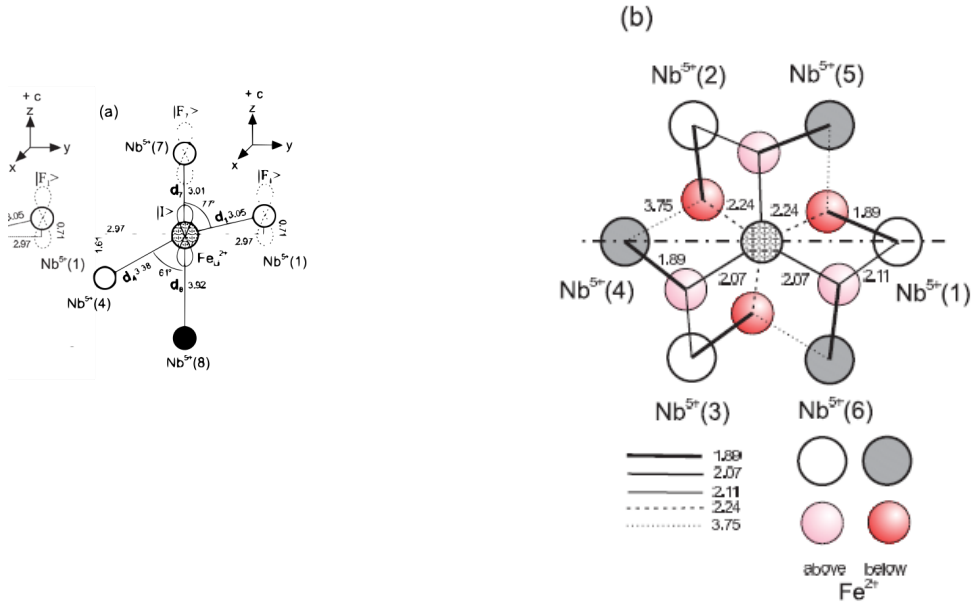

(a) (b)

Figure 3.2: Fe defect in lithium niobate structure [51]

freeing a bound electron and placing its electron in the conduction band. The Fe atom being in a Li position will see as the nearest charge source eight Nb atoms so the photoelectron will be emitted into one among this eight preferred directions as we can see in Figure 3.2.

The emission probabilities in the eight main directions from the initial i to the final f state can be obtained by following the Fermi golden rule:

$$w_{i\to f} = \frac{2\pi}{\hbar}| < f|\hat{H}_s|i > |^2\rho \tag{3.4}$$

and then

$$\frac{2\pi}{\hbar}| < f|\hat{H}_s|i > |^2\rho \propto \frac{J^2d^2}{\omega}e^{-\Delta E_{i,f}} \tag{3.5}$$

where H_s is the hamiltonian that describe the interaction, ρ is the density of states of the final configuration, J is called the transfer integral as defined by the Hubbard model [20], and d is the distance between the Fe_{Li} and one of the Nb_{Nb}.

Since the transition occurs between the same atom pairs (a Fe and a Nb atoms), these expressions can safely be assumed to be equal except for the therm d^2. Those distances are available from the crystal structure, so the relative weight of each transition in our simulation can be determined. The electron, not being scattered in the general case into a local minimum of the energy bands, will start moving in the crystal until a scattering process happens changing its energy and momentum. This process continue to happen until the electron looses all its

excess kinetic energy. At this point the lattice has enough time to deform and trap the electron in a polaron state, as explained in chapter 2. Due to abundance of regular Nb ions in the lattice, it is very likely that the electron localizes onto a regular Nb site forming a free polaron. In this condition the polaron motion is no longer a coherent quantum propagation. Instead the electron moves by thermally activated hopping according to the Holstein's hopping frequency:

$$\nu_{i,f}(r,T) = \frac{1}{2}\left(\frac{\pi}{kT\lambda_{i,f}}\right)^{\frac{1}{2}} \frac{I_{i,f}^2}{\hbar} \exp\left(-\frac{r}{a_{i,f}} - \frac{U_{i,f}}{kT}\right) \tag{3.6}$$

where λ is the reorganization energy, $I_{i,f}$ is the overlap integral of the electronic wavefunctions between the initial and final site, $a_{i,f}$ is an orbital parameter quantifying the spatial extension of the electronic wavefunction on dependence of the initial and final site and $U_{i,f}$ is the hopping activation energy. From this result, it turns out that the polaron mobility $\mu = (ea^2/kT)\nu_{i,f}$ (where $a = 3.75$Åis the Nb - Nb distance) is of the order of $10^4\,\mathrm{cm\,V^{-1}\,s^{-1}}$, much smaller than typical mobility of conduction band electrons. The goal of this section is to get an estimate of the thermalization length λ_t characterizing the mean distance travelled by the electron as a coherent state in the conduction band before being trapped in a low-mobility state. This task is quite complicated, since the photoemitted electron loses its kinetic energy mainly by random scattering processes with phonons.
The formal solution of the phonon-electron scattering process would require to solve for a certain interaction hamiltonian the problem in each point of the reciprocal lattice for each band. This task is practically impossible to perform so a different approach will here be used.
The electron-phonons behaviour will be treated thanks to a mean field electron-phonon coupling model, developed by professor Paolo Umari and not published yet. Using this model, all the interaction problem is expressed in terms of the dielectric constant of the material, which is available either from literature data, either from our ab initio modelling. Besides the dielectric constant, the model requires the energy values of the bands where the scattering process takes place, and a choice of the phonon state involved in the scattering. As a further simplifying approximations, we treated the bands in parabolic approximation and we considered only the most energetic phonons with a frequency of $100\,\mathrm{cm^{-1}}$ since our displacement energy, the energy the electron has respect to the minima of the conduction band, is very high. Results of the computation of our model are shown in **??** from which we can see that a good estimate for the relaxation time is $\tau = 3 \times 10^{-15}\,\mathrm{s}$

Knowing the dominant scattering process and the relaxation time we are now ready to estimateλ_t using a Monte Carlo approach.
We start considering an electron initially trapped on the Fe site and photoemitted by a photon. According to Figure 3.2, each electron is emitted into a randomly chosen direction among the eight possible ones, so to match the

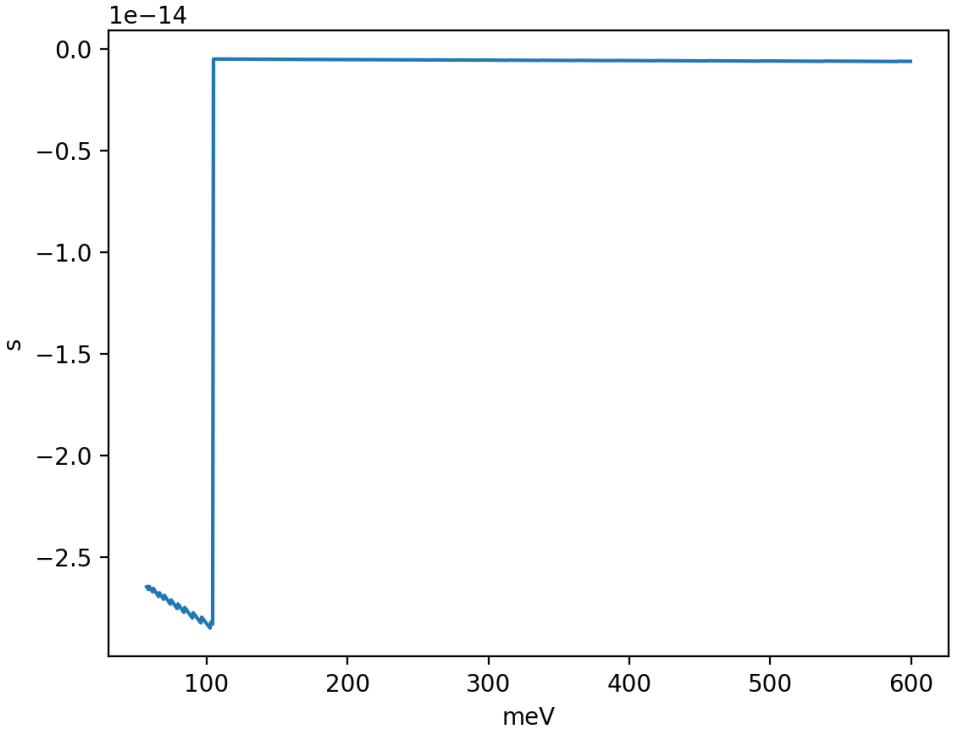

(a) Simulated relaxation time

relative probability calculated in Equation 3.5 between each of the eight directions $p_{i,j} = d_i^2/d_j^2$. For each run of this Monte Carlo simulation, an electron is generated with a fixed energy and its initial state is found inside the first Brillouin zone by determining among the possible band states those satisfying energy and momentum conservation rules. To this goal we sampled the first Brillouin zone with a 11x11x11 k-point mesh retaining the energy values of the first six conduction bands. Each band was then approximated with a parabolic interpolation at the nearest neighbour to obtain an analytical approximation of the band structure.
Since we think electrons as wave packets, and so we can write

$$\vec{v} = \frac{d\omega}{d\vec{k}} = \frac{1}{\hbar}\frac{dE}{d\vec{k}} \tag{3.7}$$

from the local derivative of the band at the point where the electron is lying, we can compute for any state its velocity. This result is combined with the scattering time τ and was used to calculate a displacement. A scattering process was then simulated: chosen a random direction a phonon was generated and solutions for both energy and momentum conservation were searched again inside the first Brillouin zone. With the updated energy and momentum for the electron, the process was then repeated until the electron energy was smaller than the phonon energy and the final displacement, corresponding to the thermalization length for the chosen direction, is recorded.

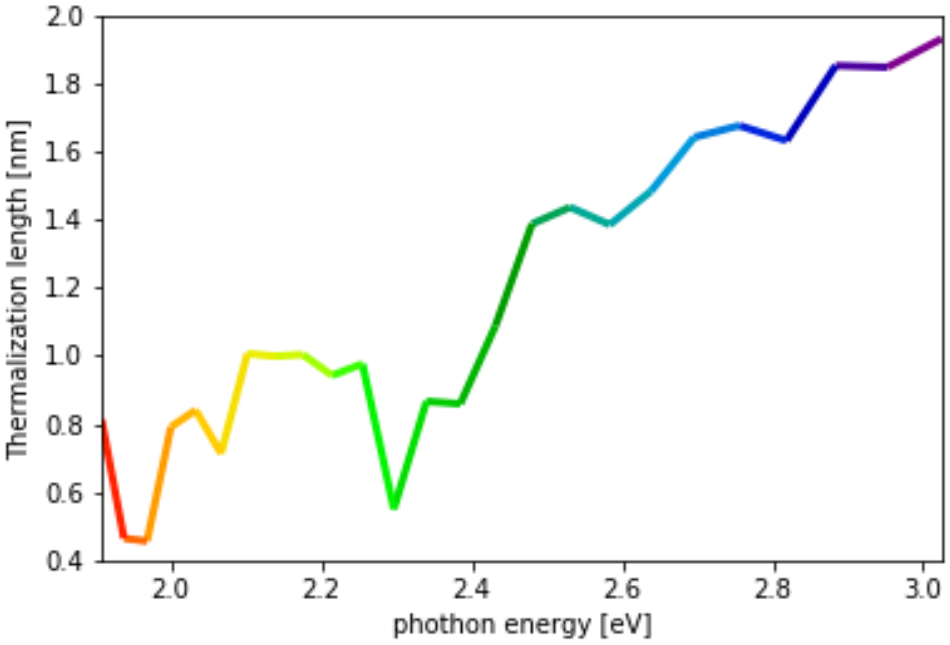

Figure 3.3: Simulated values for λ_t

In a second step the displacements along all the directions were summed to obtain the mean displacement a photon cause to an electron, which coincides with the photogalvanic length L_{PG}.
Results of the simulations,performed at various wavelengths, with 1500 total generated electrons among all eight directions, Table 3.2 while a representation of the averaged λ_t as a function of the photon energy can be seen in Figure 3.3.

The results of Figure Figure 3.3 can be directly compared with experimental results. Our calculations for different wavelengths reflect the dip of experimental data occurring around 2.3 eV, which is due to a change of the band reached by the photoexcited electron for those energies. In [23] the photogalvanic length L_{PG} at 2.28 eV was estimated in 0.14 nm in reasonable agreement with our results. On the other hand the thermalization lengths are in the 0.8-1.8 nm range. This sets the target thickness for the iron-doped films in order to observe the expected photocurrent enhancement.

wavelength [nm]	L_{PG} [nm]	λ_t [nm]
410	0.238	1.929
420	0.228	1.846
430	0.228	1.850
440	0.201	1.631
450	0.207	1.675
460	0.202	1.640
470	0.183	1.483
480	0.171	1.384
490	0.177	1.435
500	0.171	1.386
510	0.134	1.088
520	0.106	8.595
530	0.107	8.668
540	0.068	5.514
550	0.120	9.768
560	0.116	9.427
570	0.124	1.004
580	0.123	9.990
590	0.124	1.006
600	0.088	7.141

Table 3.2: Calculated values for the photogalvanic length L_{PG} and for thethermalization length λ_t

Chapter 4

Fabrication of Fe:$LiNbO_3$ thin films

Our main experimental goal in this thesis is to study the feasibility of $LiNbO_3$ devices to study the bulk photogalvanic effect at the nano-scale.
The model of such a system is a thin mono-crystalline lithium niobate crystal enclosed between two electrodes with at least one of them being a transparent medium to allow light to reach the active medium. To realize such an object represent a challenge by itself: as we have seen in **??** the characteristic thermalization length of the photoemitted charges in lithium niobate average around the nanometer and so an especially thin film is required.
In this thesis we decided to use a bottom-up approach and deposit a film of $LiNbO_3$ on a substrate. This will allow for a good control on the film thickness. The main problem to overcome is that, in order to obtain a single crystal film, we must fulfill some epitactic relation with a suitable substrate that needs also to be conductive. Various techniques exist to produce thin films, in this work we chose to explore the RF sputtering since the literature suggest that is possible to obtain optimal quality crystals by this mean.

4.1 Sputtering for thin films deposition

The sputtering process is a widely used physical deposition technique useful to create thin films thanks to an high degree of control onto the material parameter and on the thickness of the material deposited.
Physically the term sputtering refers to the ejection of microscopic particles from the surface of a material when the latter is being impacted onto by energetic particles from a gas or plasma. The impacting body transfer momentum to the bound atoms of the surface of the material causing them to break their bonds and rebound in the deposition chamber, where they fly by eventually attaching to the surface of the substrate to be coated.

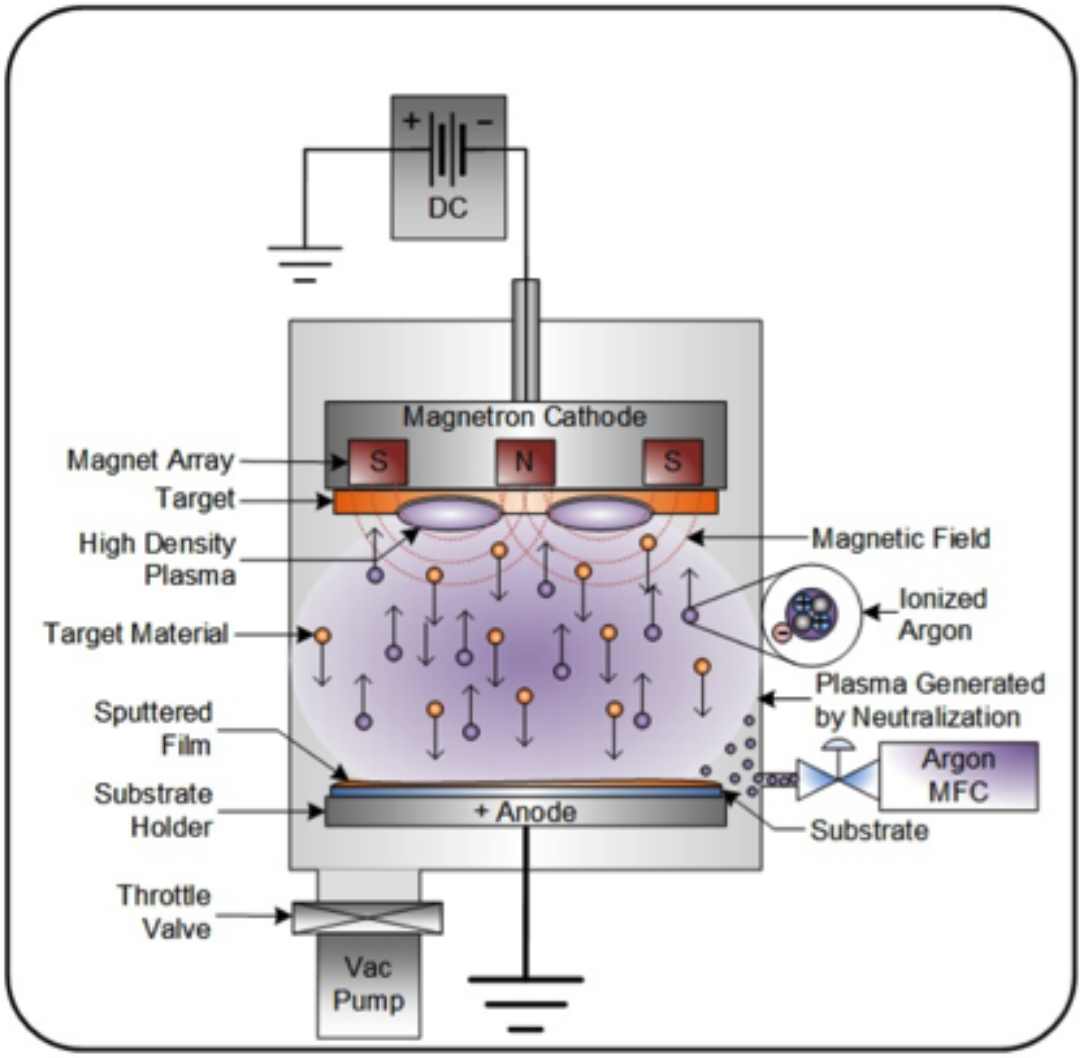

Figure 4.1: Magnetron sputtering diagram

As we can see in Figure 4.1 in a sputtering system the target and the substrate get placed respectively on the cathode and the anode of an high voltage circuit. The high potential difference cause electrons to jump off from the cathode to the anode hitting in the process gas molecules present inside the chamber and ionizing them; the newly formed ions start in turn to accelerate towards the cathode impacting on the target. The system, to avoid external contamination and to achieve in a easier way the plasma state required, is placed in a vacuum chamber that gets filled at pressure on the order of 10^{-4} mbar with an inert gas. Two variant of the just described DC sputtering worth mentioning and usually used together to achieve better results are magnetron and RF sputtering. In magnetron sputtering a magnet configuration is placed right beneath the target: being the plasma particle charged the resulting magnetic field can be used to confine the plasma near the surface of our target allowing for both a better control on the yield of the process and an evenly spread erosion of the material.

In insulating materials, this sputtering process could lead to the build up of positive charges on the surface of the target, potentially leading to an alteration or even to a complete arrest of the process. Radio Frequency (RF) sputtering exist to overcome this obstacle: an alternate radio frequency at 13.56 MHz is used instead of the DC voltage, allowing the target to discharge during each cycle. The RF sputtering comes with other two benefits that actually make it the standard way to perform sputtering deposition: firstly due to the use of an alternate voltage there is a reduced risk of an electric arc appearing in the plasma and secondly it allows for lower pressures than the DC version allowing for more efficient depositions. For our research we need to prepare a Fe - doped sample. To

4.2 Substrate choice for sputtering deposition

Since photogalvanic current in lithium niobate is inherently tied with the crystalline structure, it is necessary to achieve a nanofilm as perfect as possible, or at least strongly oriented with the c-direction pointing towards the electrode contacts. In an ideal case one would aim for an epitaxial growth of $LiNbO_3$ onto a matching substrate.
To promote such a growth the choice of an appropriate substrate is crucial and various possibilities were available. We focused our effort on materials known to act as good substrate for $LiNbO_3$ that were also transparent to visible light while also being electrically conductive.
The final choice fell onto gallium nitride (GaN) a transparent wide gap semiconductor recently at the center of an uprising interest for its promising applications, having recently become the fundamental material for green, blue, and ultraviolet electro-optic devices. GaN can be doped either with -p or -n character, so that it could be used as a transparent electrode too. GaN grows in a wurtzite configuration with lattice parameters $a = 3.189 and c = 5.156$ [4], a representation of its lattice can be seen in Figure 4.2. It is reported in literature [5] that an epitaxial growth of $LiNbO_3$ onto GaN its possible along the c-axis orientation for both crystals. An hexagonal pattern is present for both crystals in this orientation and allows for two possible dispositions of $LiNbO_3$ by rotating it respect to the lattice beneath of around 30° with a mismatch around 6.8%.
Since its application in LED production its quite easy to get a supply of GaN related wafers; we settled our choice for substrates onto 430 µm sapphire wafers with on top a 5 µm film of GaN with low numbers of dislocations. The films, see **??**, to render GaN electrically conductive, were bought doped both with positive charge donors (Mg) as well as negative ones (Si) to allow in future works the study of possible effects of charge carriers onto the bulk photogalvanic effect current extraction.

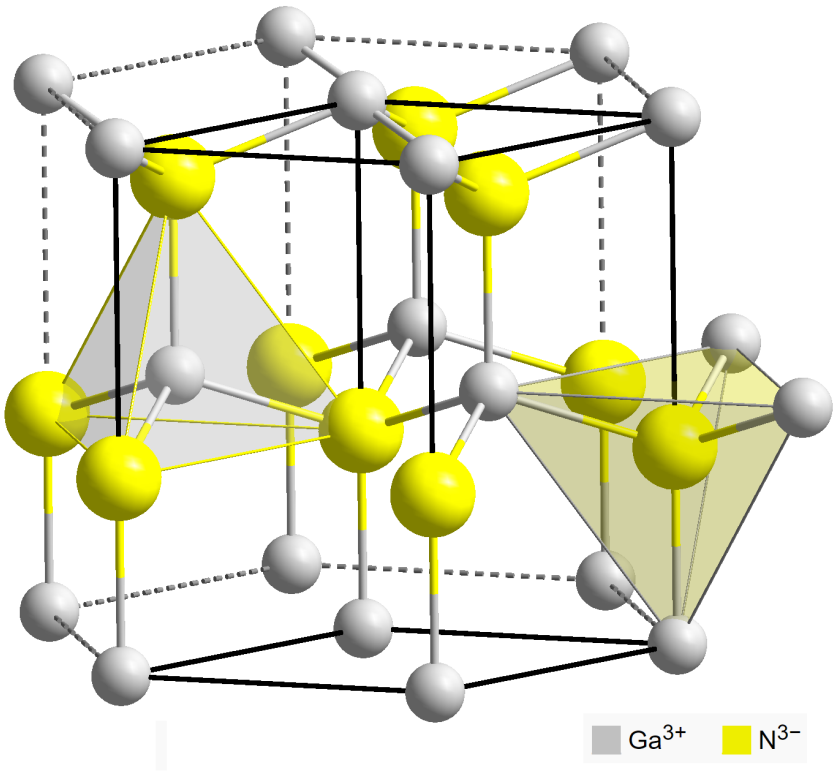

Figure 4.2: GaN crystal lattice structure

4.3 Choice of sputtering parameters

The parameters that determine the outcome in a sputtering deposition, aside from the choice of target and substrate materials, are only a few but highly dependent one from each other so a careful exploration of the possible configurations must be performed. As seen in chapter 2 the suggested optimal parameters found in literature are an RF power of 100 W, a target-sample distance of 5 cm, a plasma atmosphere of $Ar + O_2$ in a 2:1 ratio with a total pressure of around 10 mTorr, and a substrate temperature greater than 400 °C so our efforts will be focused near this values.
To fulfill the requirements for temperature and distance a pre-existing apparatus was modified setting the final values to the recommended ones; details about this modification are explained in Appendix B. The remaining free variables are now total pressure, atmosphere composition, and RF power.
RF power mainly affects the deposition rate, as an increase in the field amplitude accelerates the ions in the chamber leading to a higher sputtering yield. As a secondary effect, the kinetic energy of the sputtered species is larger as well, and this may affect the growth rate and the quality of the deposited layer. This effect can however be counter-balanced by the total work pressure in the chamber since a greater density of the gases lead to a shorter mean free path of the sputtered species, effectively slowing the particles during their travel.
To limit the number of free experimental parameters in our investigation, we decided to set the RF power to 100 W, as this is the value recommended by most of the examined literature**citazione TODO** and to study the effect of the to total pressure and atmosphere composition, since those parameters affect the growth in a much less predictable way. Their role in our work is mainly to control the Li ratio in $LiNbO_3$. In our depositions we worked at two total pressure values at 40×10^{-4} mbar and 15×10^{-4} mbar changing the the atmosphere composition.

4.4 Sample preparation

The creation of our samples required three steps: cutting the samples from commercial wafer, cleaning, and the actual sputtering deposition.
We started from two GaN on sapphire wafers of 2 inches of diameters. In both wafers the GaN film had a thickness of 5 microns over a 0.5 mm thick substrate. In order to verify a possible effect of the substrate doping on the final results, we decided to use a p-doped GaN sample and an n- doped one. The former was Mg- doped (p-GaN) and polished only on the upward face while the latter was doped with Si (n-GaN) and polished on both surfaces. The wafers were cut in samples with a diamond dicing machine realizing 10x12 mm rectangles where the long side was oriented parallel to the GaN (010) crystal direction.
After cutting, the samples were thoroughly cleaned: even the smallest smudge on the sample surface would affect the growth of our films. The cleaning procedure

Figure 4.3: Photo taken during spattering deposition. It's possible to notice the plasma being confined near the target surface in a characteristic flame shape

used is quite standard for handling hard materials that need to be polished without being scratched: samples were treated firstly with distilled water and soap, then in acetone, then in ethanol and lastly in isopropyl alcohol. Each step of the cleaning is designed to remove the traces left from the precedent one; to avoid to scratch the samples instead of cleaning them by hand they were treated with ultrasounds while bathing in the correspondent step and dried by the mean of compressed air.
For each deposition run two samples, one p-doped and one n-doped, were placed inside the chamber together to ensure that the only difference between them was the substrate itself. The final combinations used are reported in Table 4.1

Deposition	Power O_2 pressure	distance Deposition time	total pressure	Ar pressure
1	100 W 14×10^{-4} mbar	5 cm 1800 s	40×10^{-4} mbar	26×10^{-4} mbar
2	100 W 9×10^{-4} mbar	5 cm 1800 s	41×10^{-4} mbar	32×10^{-4} mbar
3	100 W 5×10^{-4} mbar	5 cm 1800 s	15×10^{-4} mbar	10×10^{-4} mbar

Table 4.1: Sputtering deposition parameters

All the explored conditions successfully resulted in the deposition of a Fe:LN film.

At naked eye the samples appeared free of defects and, in the case of double - side polished substrates, transparent. In the next paragraphs the characterization of the samples will be described in detail.

Chapter 5

Characterization procedure

We start now to work towards our characterization procedure. Our objectives are to gain some insight about the films we have deposited by the sputtering method in relation to the process parameters, and to consolidate a measurement procedure that will be useful for further studies.

5.1 Topography characterization

As a first step we will look into characterizing the thickness of the deposited films. Since the main goal of our research project is to study how the bulk photogalvanic length depends to the film thickness we need to develop a reliable experimental methodolgy to determine it and in turn to establish accurately the deposition rate.
A first method we used was a contact profilometer. In a contact profilometer a stylus, usually made out of diamond, moves across the sample while touching the surface measuring the displacement of the surface. This technique allows to obtain a line profile of the surface on a very large scan length. To allow to perform such a measure, during deposition processes, a small area of the substrates were covered with a little piece of Si: such a trick lead to the creation of a quite sharp edge between the portions of the sample with and without the film.
We performed several measurement of the samples edges in different positions to reduce the statistical error on the measure while, to reduce any possible systematic error, values were acquired both from the GaN toward the film and in the reverse direction. The obtained values are reported in Table Table 5.1
Surface morphology was then investigated with an atomic force microscope (AFM) to study the RMS roughness of the film and to characterize the growth process. In Figure 5.9 images acquired for the different deposition conditions are reported. It's very noticeable that the samples present quite different topographies according to the different deposition conditions. The measured roughnesses are quite different as well and are reported in Table Table 5.1. We will try here to

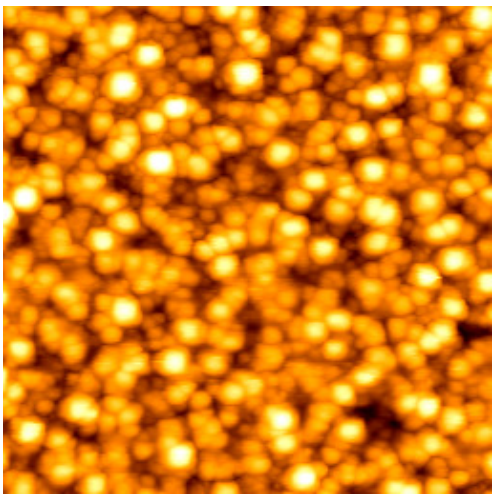

(a) Deposition 1 2x2 µm p-type GaN

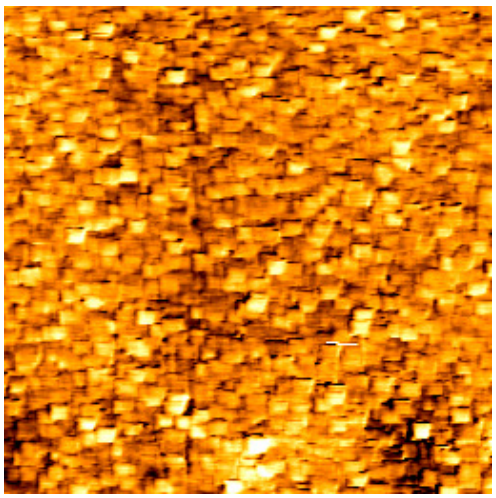

(b) Deposition 1 5x5 µm n-type GaN

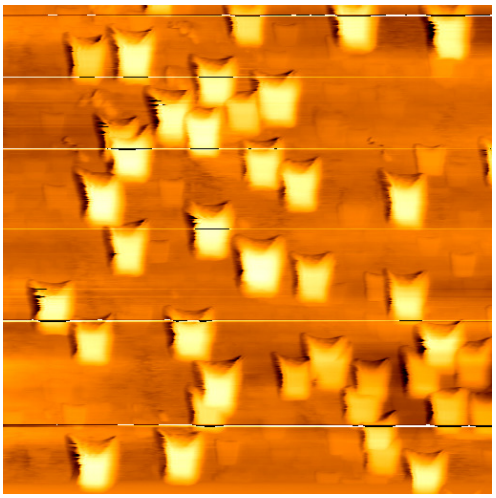

(c) Deposition 2 2x2 µm p-type GaN

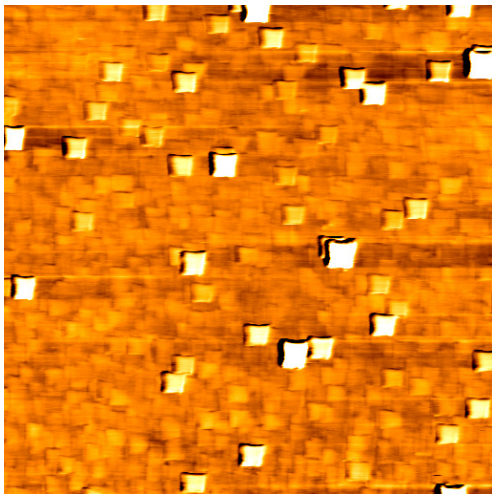

(d) Deposition 2 5x5 µm n-type GaN

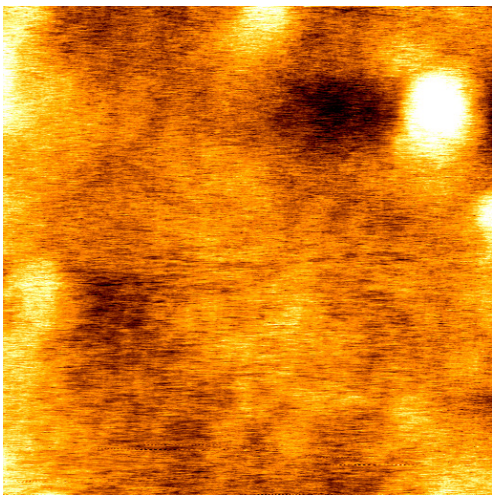

(e) Deposition 3 2x2 µm p-type GaN

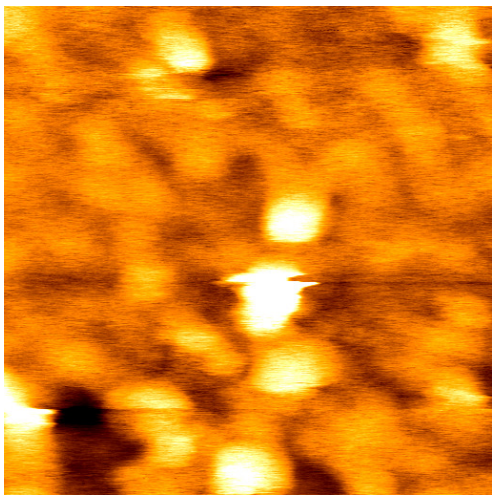

(f) Deposition 3 5x5 µm n-type GaN

Figure 5.1: Topology of the samples acquired via AFM

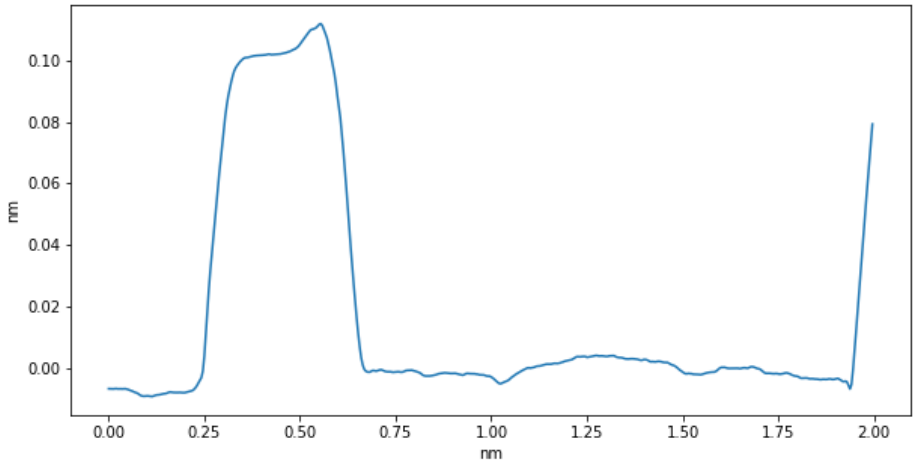

Figure 5.2: Surface line profile (Deposition 2, p-type GaN)

give an interpretation of the main differences although further study are needed. Deposition 1 shows a rough surface with a pattern that resembles a squared lattice possibly due to a Volmer-Weber growth process; such a conformation here is only hinted but becomes far more pronounced in deposition 2, as it can be seen from the RMS roughness value. Films deposited in this way present also a higher thickness. In Figure 5.2, a line scan of one of those square features obtained from deposition 2 was studied: their mean length (measured at half height) was found to be near 0.5 µm while the angle of the sides was found to be around 45°. Such a topography hints a crystalline order of the deposited film, with the observed features being probably related to some growth facets. This will be confirmed in forthcoming paragraphs by X-ray analysis. Being the difference between the deposition 1 and deposition 2 only defined by a diverse ratio in the Ar:O_2 atmosphere composition, the most likely hypotheses is that such different growth rates are related to a different composition of the crystals regarding the Li composition as explained in chapter 2; however other techniques, such as an RBS analysis would be needed to confirm such a difference.
Deposition 3 on the contrary presents a smooth surface and no real shape can be distinguished by looking on the images. The film thickness is lower as well, compared to deposition 2. Those observations suggest a re-sputtering phenomenon during the deposition. In fact Deposition 3 is characterized by a lower total pressure: in such a configuration atoms in the chamber acquire more kinetic energy due to a much longer mean free path. When the plasma becomes so highly energetic its confinement becomes less efficient and, due to the alternated voltage used, some Ar atoms can be scattered back towards the sample removing part of the film while it is being deposited.

Deposition	Substrate	LN thickness	Surface avg roughness
1	p-type	240(10) nm	1.57(1) nm
1	n-type	250(10) nm	1.68(1) nm
2	p-type	280(10) nm	30.6(1) nm
2	n-type	280(10) nm	24.0(1) nm
3	p-type	182(8) nm	0.418(1) nm
3	n-type	177(5) nm	0.804(1) nm

Table 5.1: Samples films characteristics via AFM and profilometer measurement

5.2 Optical absorption spectroscopy

The main source for the charges responsible for the bulk photogalvanic effect, as we explained in chapter 2, are the Fe_{Li}^{2+} donors. The intensity of the photogenerated current is linearly dependent on their concentration and consequently measuring it is fundamental to investigate the efficiency of the photoemission. As shown by Ciampolillo et al., it is possible to characterize the doping level in Fe:$LiNbO_3$ by the mean of the optical absorption at various wavelengths [15]. Our objective will be to characterize the optical absorption at 532 nm, as at this wavelength the total Fe_{Li}^{2+} concentration can be determined by dividing the absorption coefficient by the Fe_{Li}^{2+} cross section $3.95 \times 10^{-22}\,m^2$. In our case the measurement must be performed by crossing a multilayer sample with different refractive indexes, so that interference effects complicates the analysis. It will turn out that our analysis can provide not only the absorption coefficient, but also a precise determination of the film thickness as a useful by-product.
In Figure 5.9 a basic depiction of the apparatus used is reported. We used a Jasco V600 dual beam spectrometer. Each sample, before being measured, did undergo a standard cleaning procedure, the same described in chapter 5. For each sample, the intensity after the medium was measured as a function of the wavelength starting from 350 nm to 2500 nm at 1 nm intervals. The data acquired were normalized with respect to a reference spectrum in order to eliminate the spectral response of the light source. In this way the absolute transmission coefficient of our samples could be measured while the baseline signal was removed performing an additional acquisition without the sample. Since only n-doped GaN on sapphire substrates were available in a double side polished version, only them were measured. As the p-GaN and n-GaN samples were deposited in the same sputtering run and in the same conditions, it can be assumed that the results obtained here are valid for both the samples deposited in the same run.
For a wave propagating through an optical medium, the Lambert-Beer law states that the light intensity after crossing a material slab with thickness d is given by:

$$I(z) = I_0 e^{-\alpha_{abs} z} = I_0 e^{-\sum_i \sigma_i n_i z} = I_0 e^{-\sum_i \epsilon_i c_i z} \tag{5.1}$$

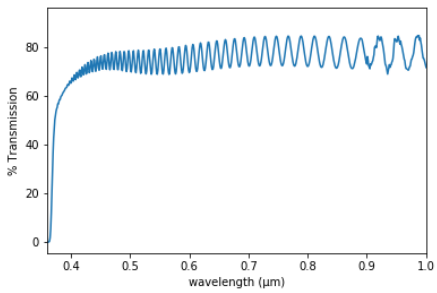

(a) Deposition 1 transmission spectrum

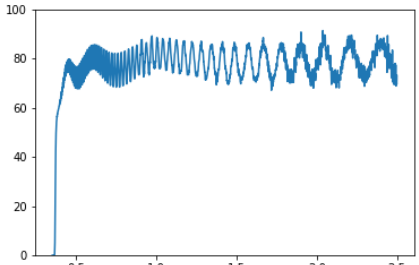

(b) Deposition 2 transmission spectrum

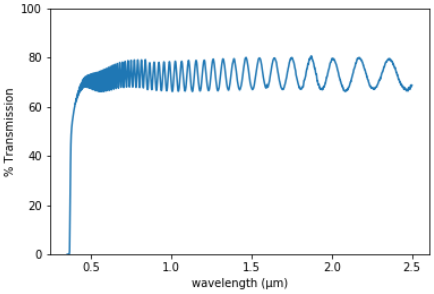

(c) Deposition 3 transmission spectrum

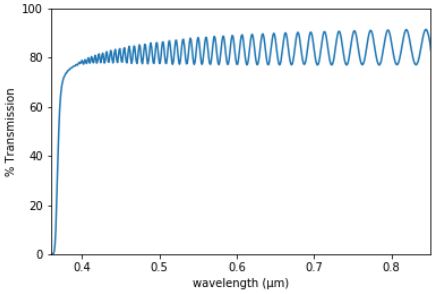

(d) Substrate transmission spectrum

Figure 5.3: Acquired spectra for optical absorption analisys

where α_{abs} is the absorption coefficient. In a transparent medium, the absorption coefficient can be related to the concentration of the impurities responsible for the electronic transitions which absorb the incoming photons. If the impurities cross section σ_i at a given wavelength is known, their concentration c_i can be inferred.

Our samples however come as a multilayered structure of three different materials each one with a different thickness and refractive index. Waves propagating through such a media will undergo thin film interference producing a rather complicated intensity amplitude figure. Since we are specifically interested in the absorption properties of $LiNbO_3$ we need to decouple the contributions of each layer to effectively measure its own absorption coefficient.
The effect of interference combined with the optical absorption of our media makes the analysis of the spectra obtained a challenge not easily solvable so let's start by ignoring the absorption. In this case by the mean of the transfer matrix method (see Appendix C) we can calculate the transmittance coefficient as a function of the thicknesses and refractive indexes of our layers.
Refractive indexes for our materials are well known in the range of wave lengths we are using and can be well modeled by the Sellmeyer equation [17] [18] [19] effectively removing them from the pool of parameters that needs to be estimated. The thickness of the different layers has a strong influence on the fringes

observed in the transmission spectrum. In figure Figure 5.4 an example of simulated transmission spectrum obtained by the matrix method is shown. As it can be seen, the fringe visibility is much higher than the experimentally observed one and this is due to the fact that the matrix method considers perfectly coherent light, while in our experiment the optical probe, obtained by an incandescent lamp has a finite coherence length. Moreover, the absorption of our samples modulates the intensity of the transmitted signal as a function of the wavelength. Nevertheless, the maxima and minima positions are affected only by the thicknesses of the layers, so that a least square regression of the transmittance coefficient can still be performed to effectively measure the mean thickness of our films.
To reduce the error on our estimation process we firstly considered a sample with no lithium niobate on it; we saw that to correctly obtain a function with the same periodicity of our sample, only the GaN layer was required while the Sapphire substrate could be safely neglected: since larger layers produce fringes with smaller spacing and due to the high transparency of Sapphire the effect of this layer is basically indistinguishable from a noise on our spectra. The estimation procedure returned for the GaN film a thickness of 5.5754(6) µm well compatible with the nominal thickness of 5 µm. The thickness of the GaN film was fixed to this value in the rest of the analysis. Moving to transmission spectra of LN/GaN/Sapphire samples, we added in the model an additional layer of lithium niobate. Leaving its thickness as sole free parameter, we derived for each sample the transmission coefficient and effectively the thickness of the $LiNbO_3$ coating on them. In Figure 5.4 a comparison between the data acquired and the correspondent calculated transmittance coefficient is reported while the estimated value can be find in Table 5.2. The values are in qualitative agreement with those obtained from profilometric data; the quantitative differences can be ascribed to the fact that the profilometric data suffer from the specific shape of the step as defined by the mask and the deposition process. We believe that the thickness determination hereby obtained, being averaged on the footprint of the optical beam and in the center of the sample is more reliable.

To extend the transfer matrix method in the case of absorbing media is not an easy task so we developed a 'single ray' approximation for our problem. If we consider a ray that propagates trough our multilayer without performing any thin film interference, but being subjected to an absorption, its intensity after the structure can be written as:

$$I = I_0 T e^{-\alpha_1 d_1 - \alpha_2 d_2 - \alpha_3 d_3} \tag{5.2}$$

where T is obtained by multiplying the transmission coefficient in absence of absorption (i.e. due to each optical interface the ray pass trough). We will call this ray the *single ray intensity*.
In general, for two interfaces defining an optical layer, a passing beam is partially reflected. This secondary beam can propagate back to the previous interface, where is reflected again in the forward direction and can eventually interfere with our first ray. Let us consider such a ray and take the case were the reflections

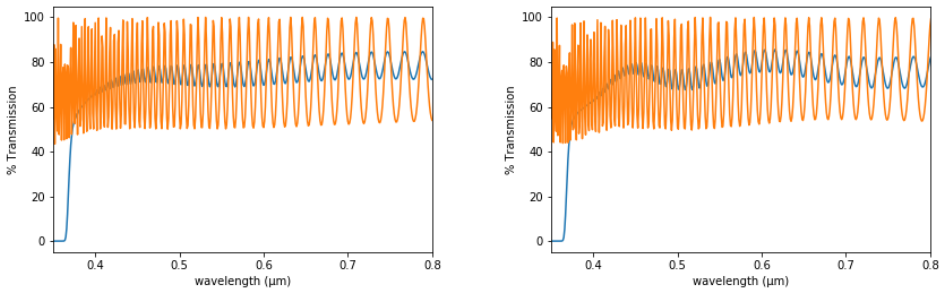

(a) (b)

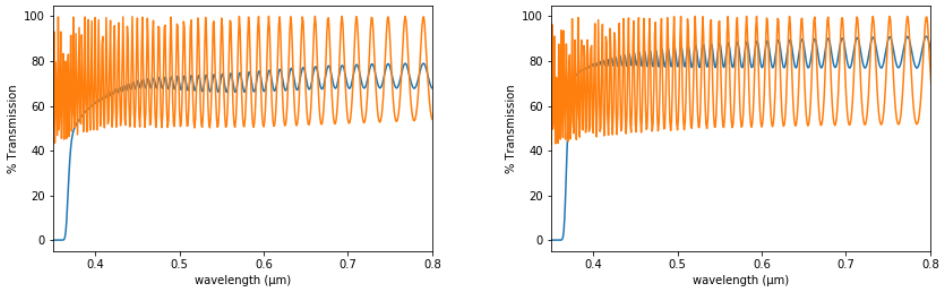

(c) (d)

Figure 5.4: Comparison between acquired spectra and Transmission coefficient calculated via transfer matrix method

happen inside, for example, the second layer. We can write the above - mentioned situation as:

$$I = I_0 T e^{-\alpha_1 d_1 - 3\alpha_2 d_2 - \alpha_3 d_3} (r_{2,3} r_{2,1})^2 \cos\left(\frac{4\pi}{\lambda} n_2 d_2\right). \tag{5.3}$$

However, the situation is more complex because the reflection process can occur indefinitely on each of the layers. Thus, if we define now $\tau_i = (r_{i,i+1} r_{i,i-1})^2$ and $\phi_i = \frac{4\pi}{\lambda} n_i d_i$, we can write for the total intensity that exit the multilayer:

$$I_{th} = I_0 T e^{-\alpha_1 d_1 - \alpha_2 d_2 - \alpha_3 d_3} \sum_{i,j,k=0}^{\infty} \sum_{l=0}^{n_l} \sum_{m=0}^{n_m} \tau_1^i \tau_2^j \tau_3^k t_{1,2}^{2l} t_{2,3}^{2m} e^{-2i\alpha_1 d_1 - 2j\alpha_2 d_2 - 2k\alpha_3 d_3} \cos(\Phi_{i,j,k}). \tag{5.4}$$

with $\Phi_{i,j,k} = i\phi_1 + j\phi 2 + k\phi_3$ and where the numbers n_l, n_m are the maximum number of allowed transitions trough an interface for a reflected ray at a certain combination of i, j, k.
Let's suppose now that the absorption process applies only to the principal component, i.e. only the first time the light travel through a layer, than we could write:

$$I^* = I_0 T e^{-\alpha_1 d_1 - \alpha_2 d_2 - \alpha_3 d_3} \sum_{i,j,k=0}^{\infty} \sum_{l=0}^{n_l} \sum_{m=0}^{n_m} \tau_1^i \tau_2^j \tau_3^k t_{1,2}^{2l} t_{2,3}^{2m} \cos(\Phi_{i,j,k}). \tag{5.5}$$

This expression, when

$$\sum_{i,j,k=0}^{\infty} \sum_{l=0}^{n_l} \sum_{m=0}^{n_m} \tau_1^i \tau_2^j \tau_3^k t_{1,2}^{2l} t_{2,3}^{2m} \cos(\Phi_{i,j,k}) = 1 \tag{5.6}$$

coincide with the *single ray intensity* we found before so we call *single ray approximation* the assumption that when this condition is satisfied one could write $I_{th} = I^*$.
If this holds true then we can get the absorption coefficients of our materials as

$$\alpha_1 d_1 + \alpha_2 d_2 + \alpha_3 d_3 = -\log\left(\frac{I^*}{I_0 T}\right) \approx -\log\left(\frac{I_{th}}{I_0 T}\right) \tag{5.7}$$

Let's see if we can get an estimate of the error performed by such an approximation.

$$\frac{I_{th}}{I_0 T} = e^{-\alpha_1 d_1 - \alpha_2 d_2 - \alpha_3 d_3} \sum_{i,j,k=0}^{\infty} \sum_{l=0}^{n_l} \sum_{m=0}^{n_m} \tau_1^i \tau_2^j \tau_3^k t_{1,2}^{2l} t_{2,3}^{2m} e^{-2i\alpha_1 d_1 - 2j\alpha_2 d_2 - 2k\alpha_3 d_3} \cos(\Phi_{i,j,k}) \tag{5.8}$$

We can expand $e^x = 1 + x + o(x^2)$ so our expression become

$$\frac{I_{th}}{I_0 T} \approx e^{-\alpha_1 d_1 - \alpha_2 d_2 - \alpha_3 d_3} \left[1 + \sum_{i,j,k=0}^{\infty} \sum_{l=0}^{n_l} \sum_{m=0}^{n_m} \tau_1^i \tau_2^j \tau_3^k t_{1,2}^{2l} t_{2,3}^{2m} (-2i\alpha_1 d_1 - 2j\alpha_2 d_2 - 2k\alpha_3 d_3) \cos(\Phi_{i,j} \right. \tag{5.9}$$

where the first term is simply equal to one because we are in the points defined by Equation 5.6. By taking the logarithm now we can see that the error we commit on the estimate of our absorption coefficients is given by

$$\epsilon = \left| \log \left[1 + \sum_{i,j,k=0}^{\infty} \sum_{l=0}^{n_l} \sum_{m=0}^{n_m} \tau_1^i \tau_2^j \tau_3^k t_{1,2}^{2l} t_{2,3}^{2m} (-2i\alpha_1 d_1 - 2j\alpha_2 d_2 - 2k\alpha_3 d_3) \cos\left(\Phi_{i,j,k}\right) \right] \right| \tag{5.10}$$

$$\approx \left| \left[\sum_{i,j,k=0}^{\infty} \sum_{l=0}^{n_l} \sum_{m=0}^{n_m} \tau_1^i \tau_2^j \tau_3^k t_{1,2}^{2l} t_{2,3}^{2m} (-2i\alpha_1 d_1 - 2j\alpha_2 d_2 - 2k\alpha_3 d_3) \cos\left(\Phi_{i,j,k}\right) \right] \right| \tag{5.11}$$

Since all the τ_i are positive numbers smaller than $1/2$ and all the $t_{i,j}$ are positive numbers smaller than 1 the dominant term for the error is

$$\epsilon_p = 2\left(\tau_1\alpha_1 d_1 + \tau_2\alpha_2 d_2 + \tau_3\alpha_3 d_3\right) \left|\cos\left(\Phi_{i,j,k}\right)\right| \tag{5.12}$$

For our refraction indexes and in our range of wavelengths the biggest of the τ_i is τ_2 so we can write

$$\epsilon_p \leq 2\tau_2\left(\alpha_1 d_1 + \alpha_2 d_2 + \alpha_3 d_3\right) \left|\cos\left(\Phi_{i,j,k}\right)\right| \tag{5.13}$$

and computing the relative error on the estimate we get

$$\epsilon_{r_p} \leq 2\tau_2 \left|\cos\left(\Phi_{i,j,k}\right)\right| \leq 0.02 \tag{5.14}$$

where the final estimate is done by taking the maximum value of τ_2 and by taking the cosine equal to 1.

We have successfully demonstrated that our approximation is valid we now need only to determine for which values of λ the condition is satisfied. Since we have the general expression of the transmission coefficient thanks to the transfer matrix method when no absorption is present and since it's quite easy to calculate the transmission coefficient for a single ray by the mean of the Fresnel coefficients we just need to find those points where the two are equal.

In Figure 5.5 a confront for one of our samples experimental data and its two calculated transmission coefficient is reported. For each intersection between the two coefficients the corresponding value for our sample was found and from it we calculated the attenuation exponent that we can see in Figure 5.6.

These set of values can now be fitted to find the absorption peak at 532 nm and by subtracting from each sample curve the absorption exponent find for the substrate we can access directly the term relative to lithium niobate.

Remembering now that for Lambert-Beer relation $\alpha = \sigma n$ by dividing the height of the peak we have measured by the $\mathrm{Fe}^{2+}_{\mathrm{Li}}$ cross section that is equal to $3.95 \times 10^{-22}\,\mathrm{m}^2$ [15] we are able to estimate the density of Fe^{2+} in the crystal and their percent concentration.

A summary of the values measured for our data can be found in Table 5.2. The obtained values indicate a doping level of few molar percent, which is quite high. This can be explained by the fact that procedure of poisoning the target with some Fe pieces was more effective than expected.

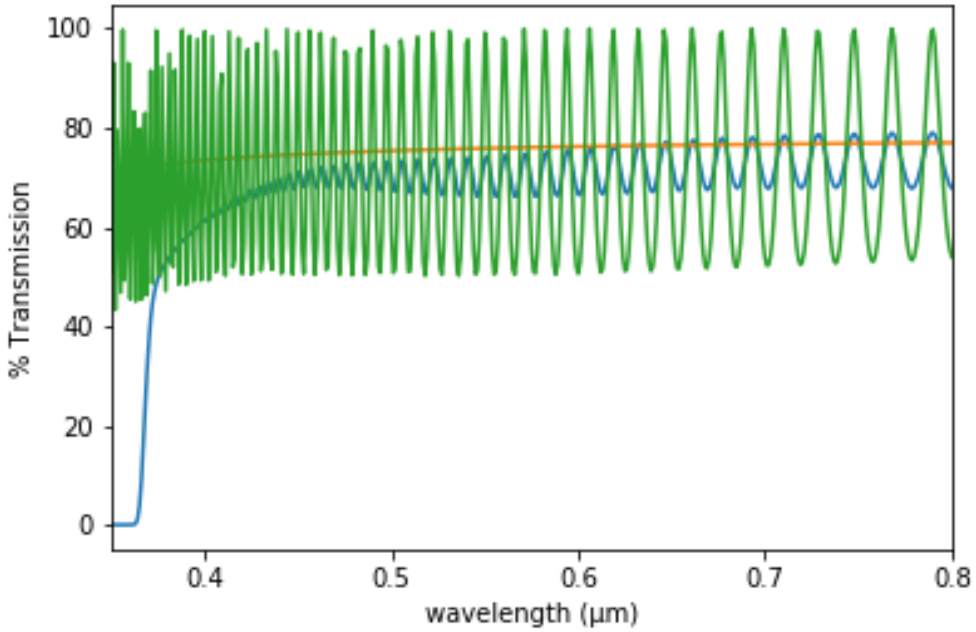

Figure 5.5: Confront between experimental data and the two different transmission coefficients for deposition 3. The intersections between the green line and the orange one are the points for whom the *single ray approximation* is satisfied. The absorption of our sample can be estimated by confronting them with the correspondent measured value.)

Deposition	LN thickness	Absorption peak position	Fe^{2+} concentration
1	126.2(6) nm	550(10) nm	4(1) %
2	224.5(7) nm	500(10) nm	5.7(8) %
3	128.3(6) nm	550(10) nm	3.2(8) %

Table 5.2: Caption

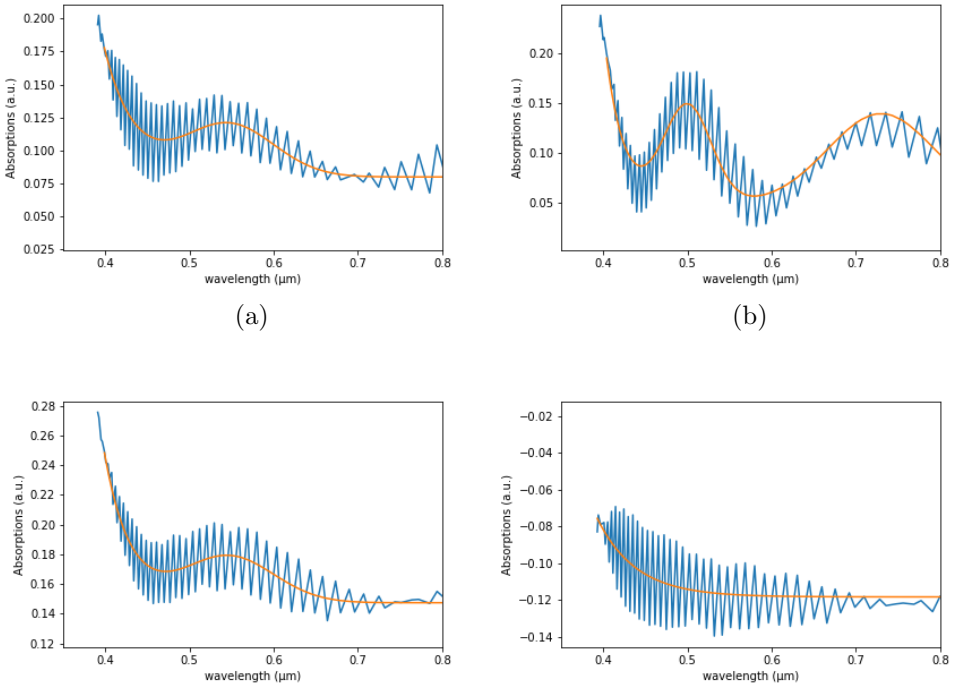

Figure 5.6: Absorption interpolation

5.3 High-Resolution XRD analysis

When studying crystalline thin films X-ray diffraction is one of the most powerful tools one can use. This set of techniques has been long known in particular in the semiconductor industry to provide an highly accurate characterization of the crystal lattice providing in multilayered systems information about thickness, composition, and strain of each layer. In an XRD experiment, the crystal structure is investigated by sending an x-ray radiation, with a wavelength similar to crystal interplanar spacing. In this case the method of Reciprocal Space Mapping (RSM) is especially useful. It consists in preparing the incident beam so that it can be approximated as a plane wave with wavevector $\mathbf{k}_0$ and using a highly angle-resolved detection system so that the measured intensity can be attributed to a precise component with wavevector $\mathbf{k}_f$. In these conditions we can plot the measured intensity as a function of the scattering vector $\mathbf{Q} = \mathbf{k}_f - \mathbf{k}_0$. It can be shown that the Bragg's law

$$n\lambda = 2d\sin(\theta). \tag{5.15}$$

implies that the crystal fulfill the diffraction conditions relative to a crystallographic plane family when the scattering vector falls upon the reciprocal lattice point associated to the chosen plane family. Therefore the scattering vector $\mathbf{Q}$ is the 'probe' used to investigate the reciprocal lattice and its length and direc-

tion can be altered by changing the directions of $\mathbf{k}_0$ and $\mathbf{k}_f$ by means of the goniometer's angles ω and 2θ. ω is the angle at which the incident beam meets the sample surface (the value of ω will differ from that of θ, the angle at which the incident beam meets a crystal plane, when the planes are not parallel to the sample surface). In our experiment we used a Philips MRD diffractometer equipped with a four-bounce Bartels monochromator and a parabolic multilayer mirror ensuring a highly monochromatic beam with a divergence of 0.0034 degrees in the equatorial plane and a spectral purity $\Delta\lambda/\lambda = 10^{-5}$. The $\mathrm{Cu}_{K\alpha}$ radiation of a copper anode tube operated at 40 mA, 40 kV produces X-ray radiation at a wavelength $\lambda = 1.54056\mathring{A}$. The sample is mounted on a Eulerian cradle allowing to set the desired crystal planes in diffraction condition. Both the sample and the detector, in particular, are mounted on two co-axial high precision goniometers (accuracy of 0.0005 degrees) controlled by a computer program to perform an exploration of the reciprocal space. The detector is a Xe proportional counter mounted after a Ge (2 2 0) three - bounces analyzer, with an angular acceptance of 0.0034 degrees. It is also possible to use an "open" detector without any analyzer in order to optimize the sample alignment before performing the actual measurement. The high degree of precision we manage to reach with this technique however comes at the price of a strong reduction of the intensity of the incident beam an thus the need of long acquisitions times to reach an appropriate statistic on the data we collect.
Between reciprocal and real space an inverse relation exist so while directions are held constant, the magnitude of the vectors changes inversely with respect to the interplanar spacing. Therefore, by searching for diffraction maxima around the crystal, information about the lattice can conversely be extracted.
The deformation state of our film can be characterized by comparing it to the lattice parameters of "ideal" lithium niobate. To this aim we define the *mismatch tensor*, a rank two tensor with 9 components. Its diagonal components are defined by:

$$\xi_{ii} = \frac{a_{L,i} - a_i}{a_i} \tag{5.16}$$

where the actual lattice constants of the layer are compared to those of the undistorted LN lattice along the i axis. Off-diagonal components of ξ_{ij} indicate a difference in the angles of the elementary cell. In the cases of rhombohedral and hexagonal symmetry, which are of main interest here, the suitable orthogonal coordinate system will be used, as reported in chapter 2. Measuring the deformations of the diffraction maxima of our films respect to the ones of a reference bulk lithium niobate crystal can be obtained by comparing the position of the film reciprocal lattice point, determined with the help of reciprocal space maps, with respect to those of the reference lattice. Naming $\mathbf{\Delta Q} = \mathbf{Q_L} - \mathbf{Q}$ the vector distance in reciprocal space for a chosen (h, k, l) Bragg reflection it can be shown that:

$$\Delta Q_{\parallel} = -\xi_{\perp,\parallel} Q_{\perp} - \xi_{\parallel,\parallel} Q_{\parallel} \Delta Q_{\perp} = -\xi_{\perp,\perp} Q_{\perp} - \xi_{\parallel,\perp} Q_{\parallel} \tag{5.17}$$

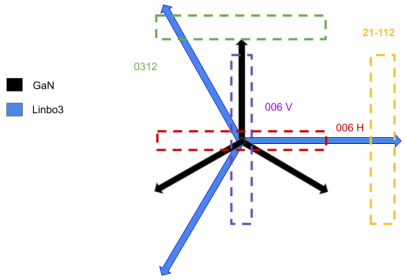

Figure 5.7: Lattices orientation and reciprocal space maps

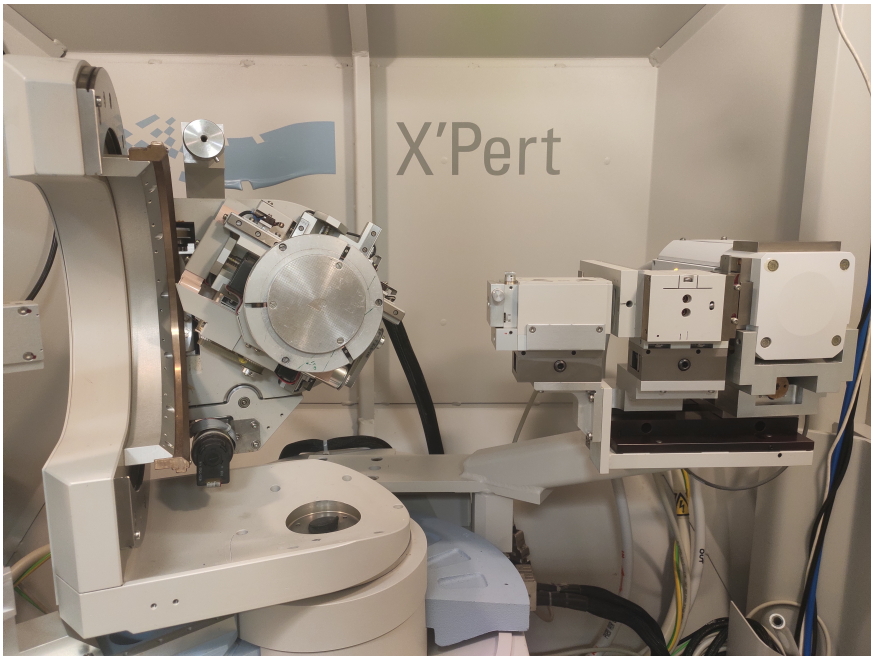

Figure 5.8: High Resolution XRD appartus

where $\Delta Q_{\parallel}$ and $\Delta Q_{\perp}$ are the componenents of the vector distance parallel and perpendicular respectively to the sample surface in the plane of the map. By measuring a number of different reciprocal space maps with independent components, one can try to setup a system of equations where the unknowns are the components of the tensor $\xi_{i,j}$. In Figure 5.8 a graphical representation of the orientations of $LiNbO_3$ and GaN along with the position and orientation of the reciprocal space maps chosen is depicted while in Figure 5.9 the maps belonging to the film created in deposition 1 on n-type GaN are reported as an example of the data acquired in this section. Each lithium niobate map is presented along the correspondent nearest GaN diffraction peak used in the alignment phase. The $LiNbO_3$ peaks we measured across the samples, as we can see, are very narrow peaks, typically with a FWHM of $0.03\,\text{Å}^{-1}$ along both directions indicating an exceptionally high crystal quality.
As we said two possible orientation for epitaxial $LiNbO_3$ on GaN are possible defined by a 30° in plane rotation of the film respect to the substrate both clock-

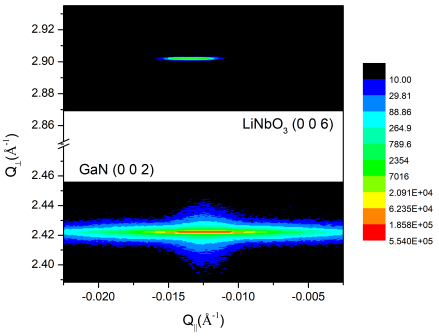

(a) (0 0 6) Vertical

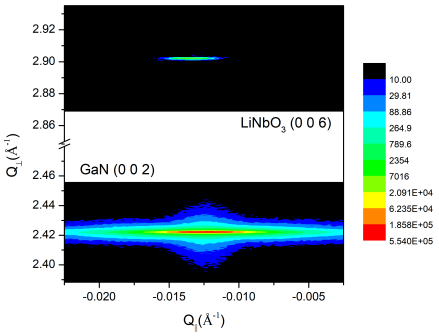

(b) (0 0 6) Horizontal

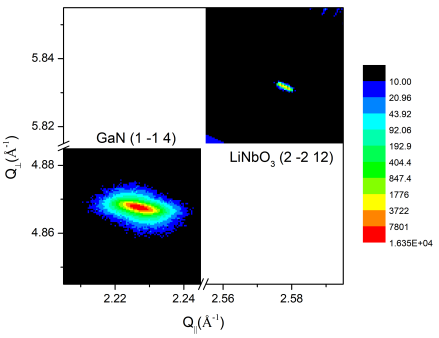

(c) (2 -1 1 12)

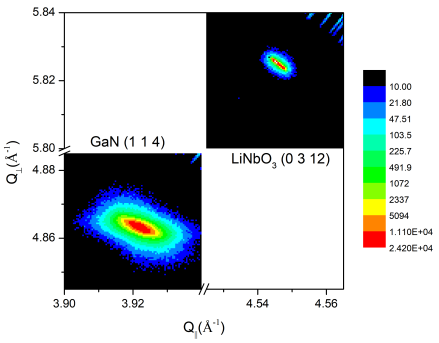

(d) (0 3 1 12)

Figure 5.9: Acquired reciprocal space maps by HRXRD, please note that there is an interruption on the axis, the maps in each image are far more distant one from each other

ξ_{xx}	-0.00881 ± 0.0006
ξ_{yy}	-0.00881 ± 0.0006
ξ_{zz}	(-0.0669 ± 0.0008)
ξ_{xz}	~ 0
ξ_{zx}	~ 0
ξ_{yz}	~ 0
ξ_{zy}	~ 0

Table 5.3: Mismatch tensor determination for the deposited films.

wise or anticlockwise. This prediction was verified to be true by a ϕ-scan of 360° after locking onto one of the asymmetric peaks: since lithium niobate has a threefold plane symmetry one should expect to see three maxima during the scan, for a bulk crystal, however six of them are found correctly spatiated by 60° one from each other compatibly with the hypothesis of two orientations being present.
Lithium niobate diffraction peak positions where then referred to their relaxed known values and used to compute the deformations on the lattice components: all samples, regardless than their deposition conditions or the type of substrate used were found to be equal one to each other within the error, so here we report a table of the different measured deformations for all the samples:

As it can be seen the films present only normal deformations and no shear components. Vertical deformation of the cell was found to be constant among all samples at $-6.69(8)\,\%$. Horizontal deformation too, defined as the mean between the deformation along the x and y axis, resulted pretty much identical among all the samples averaging at $-8.81(6)\,\%$. The absence of any meaningful difference across the samples suggest the conclusion that all samples are equal from a compositional point of view or that the difference induced is too small and is currently being masked by some other effect.
As a further step, we can try to verify whether the observed mismatch tensor is consistent with elasticity theory. Assuming a plane stress model in which all the stress is acting parallel to the interface, we can derive two Poisson relations for Lithium Niobate that read

$$\xi_{xx} - \xi_{yy} = -\frac{(\xi_{yz} + \xi_{zy})}{2}\frac{s_{44}}{s_{14}}$$

$\xi_{zz} = -2\frac{s_{13}}{s_{33}}\frac{(\xi_{xx}+\xi_{yy})}{2}$(5.18). The first one is well verified within errors, confirming that in-plane deformations are indeed practically equal. This is something that is reasonable in view of the three-fold symmetry that both GaN and Lithium Niobate possess in the interface plane. The second relation, instead is not well verified. This can be explained considering that the observed mismatch tensor is the result of two effects: an elastic deformation induced by the in-plane stress plus an "intrinsic" difference of the film lattice with respect to the one of bulk

lithium niobate. Unfortunately we could not determine the lattice parameters of the film in the relaxed state, as it is customary to do with semiconductor heterostructures because in the case of lithium niobate the elastic tensor contains too many independent component that, even from the full knowledge of the mismatch tensor it would not be possible to extract the lattice paramters in the relaxed state. Finer models and investigations are surely needed to be able to explain this excessive deformation of the crystal however our main suspect lies on the Fe doping process. The previous section showed how our crystal possess high values of Fe^{2+} impurities: the total content of Fe in the crystal is for sure higher than that so our films are very far from a near stoichiometric or a congruent lithium niobate crystal. This voids our analysis since all the elastic properties and the values of the coefficients for the relation between cell parameter and concentration of Li are given near those conditions.

Chapter 6

Conclusions

In this work a broad approach towards the feasibility of ultra-thin films of lithium niobate (polar quantum wells) and their potential application to study $LiNbO_3$ bulk photogalvanic effect in nano-system was taken. We focused on developing a procedure to produce and characterize the thin films as well as a theoretical study on the properties of the photogalvanic current this material can generate. The growth of thin films of lithium niobate was achieved by an RF sputtering methods on a GaN on Sapphire substrate focusing on the production of an high doped Fe:$LiNbO_3$. Gallium nitride was chosen as an adapt substrate because its lattice is compatible with the one of $LiNbO_3$ potentially allowing for an epitaxial growth of the films. On top of that, Gallium nitride comes as a semiconductor that is possible to dope both p and n and can be so used an electrode on the lithium niobate film to gather the photogalvanic current.
Deposition conditions for the sputtering process were studied near the values suggested by the literature, studying both a change in the atmosphere composition in the sputtering chamber as well as a change in the total working pressure. We successfully produced several heterostructures with a typical thickness between 100 and 200 nm. This technique can thus be used to tune the size of the film down to a range of few nm by suitably adapting the deposition time. Investigating samples surfaces by atomic force microscopy showed for some of the explored process conditions the presence of truncated pyramids with a square basis. This is probably related to a crystalling growth with some growth facets exposed, which hints for a Volmer-Weber growth. The presence of the pattern is not fully understood with respect to the crystalline orientation of the grown film, which, as determined by HRXRD is strongly oriented with the three-fold axis perpendicular to the film surface. For lower percentages of O_2 in the chamber these square islands resulted higher and more defined, while the thickness of the film is higher than in the previous case, suggesting that these conditions favor a faster growth. Lowering the total pressure in the chamber lead to a thinner and much flatter film that didn't show the presence of the same surface pattern as before. Rather than having removed the cause of this characteristic growth we are prone to believe that a re-sputtering of our samples by the Ar atoms took

place during the deposition.
In summary, our study allowed to determine the best parameters for the depositions were an RF power of 100 W, a sputtering distance of 5 cm, a total pressure of either 15 or 40 mbar, an Ar:O_2 near either 2:1 or 4:1.
All samples fabricated possessed an excellent crystallinity as shown by XRD characterization procedure. All our samples are characterized by a certain amount of strain, due to the considerable mismatch between GaN and $LiNbO_3$ lattices. However, by analyzing the strain state of the film, we showed that the hypothetical relaxed lattice of our film cannot have the same lattice parameters of congruent lihtium niobate. This can be attributed to compositional effects to be better studied in future works with the help of some compositional analysis (e.g. RBS).
Optical absorption measurement on the samples allowed to characterize the thickness of the produced films relying to an interpolation of the transmission coefficient calculated with the transfer matrix method. To allow for the use of the Lambert-Beer law an approximation to calculate the multilayer intensity even for absorbing media was developed and used to show that the samples we produce contained a high amount of Fe^{2+}, which should favor the study the photogalvanic effect being this ion the source of the effect in lithium niobate.
Neither crystal film quality neither surface properties of the sample were find to be dependant on the type of dopant present in the substrate's GaN film. From a theoretical point of view, the mean thermalization length and the photogalvanic length of photoemitted electrons was estimated by combining an *ab initio* simulation of the bulk structure of lithium niobate, a mean field model to estimate the relaxation time of the electrons in the crystal, and a Monte-Carlo simulation of the photo emission. The values we calculated resulted to be in good agreement with existing experimental data for the photogalvanic length L_{PG} at 2.28 eV and place themselves as a result not present at the moment of the writing in literature and will surely be fundamental for further studies on this topic.
Being this thesis only a starting point for a project on lithium niobate Bulk photogalvanic effect further studies are much more needed. Lithium niobate is a material whose properties are strongly dependent both on the doping level and the level of stoichiometry of its bulk so highly accurate procedures to verify composition of the samples are needed such an RBS analisys. Characterization performed with optical absorption, although powerful, need to be developed more possibly to the point were its possible to explain the full behaviour of the transmission coefficient without the use of our approximation.
Natural follow up of this work towards the study of the photogalvanic properties of lithium niobate would be to investigate the electric properties of $LiNbO_3$ thin films, design an optimal apparatus to measure the photocurrent at various wavelengths, and to create samples with various thicknesses to study the effect of quantum confinement and ballistic electrons extraction on the current.
The optimal crystal quality of the films obtained using the GaN as a substrate is relevant also to other possible applications of lithium niobate thin films such as ferroelectric memories so an investigation of the semiconductor/ferro-oxide

interface that originates between the two could be an interesting path to pursue. To summarize we managed to produce high crystal quality thin films identifying the optimum region of the sputtering parameters. A characterization procedure for our samples was developed although further development is still needed in particular regarding the composition of the films. A new estimate for both the thermalization length λ_t and the photogalvanic length L_{PG} was produced by the mean of a simulation process an was find highly compatible with experimental data.

Appendix A

Convergence study for DFT calculation

Running a DFT simulation means computing several times the kohn sham equations and could become a very heavy task for any machine. To speed up the computation it's useful to use Fourier Transform to hop in and back the reciprocal space since half of the terms of Kohn-Shams equations are diagonal in reciprocal space while the others are diagonal in the regular one.
Reciprocal space computations is simplified by approximating the integrals taking the functions values only on some points instead the full first Brillouin zone. The usual approach is to define a mesh of k-points and use them in our computations. The higher the number of points the more accurate our calculation will; the natural tradeoff of a dense mesh is that for an higher number of points the computational times grows as n^2.
Regular space in DFT computation is used to compute the external potential interaction i.e. the potential due to the nuclei of the crystal lattice. The Coulomb potential of an atom nucleus has a divergence for $r \to 0$ that in a computation may cause numerical problems. Overcoming this problem can be done in several ways the most common being decomposing the interaction with a plane wave expansion and approximating the computation only with the ones up to a certain energy threshold. As before a low energy will mean a faster computation but will lead to a less accurate estimate: the physical meaning of limiting the energy of the plane waves equals to obtain a potential that is not accurate under a certain range from the nucleus.
For the law of diminishing returns we can find an optimal equilibrium between the accuracy of our simulations and the time spent on them. We performed a study of the convergence of the simulation as a function of both the number of k-points and the pseudo-potential energy cut. Results of this studies can be seen in Figure A.1 and Figure A.2 and led to the final choice of 100 Ry for the energy cut and a mesh of 4x4x4 special k-points.

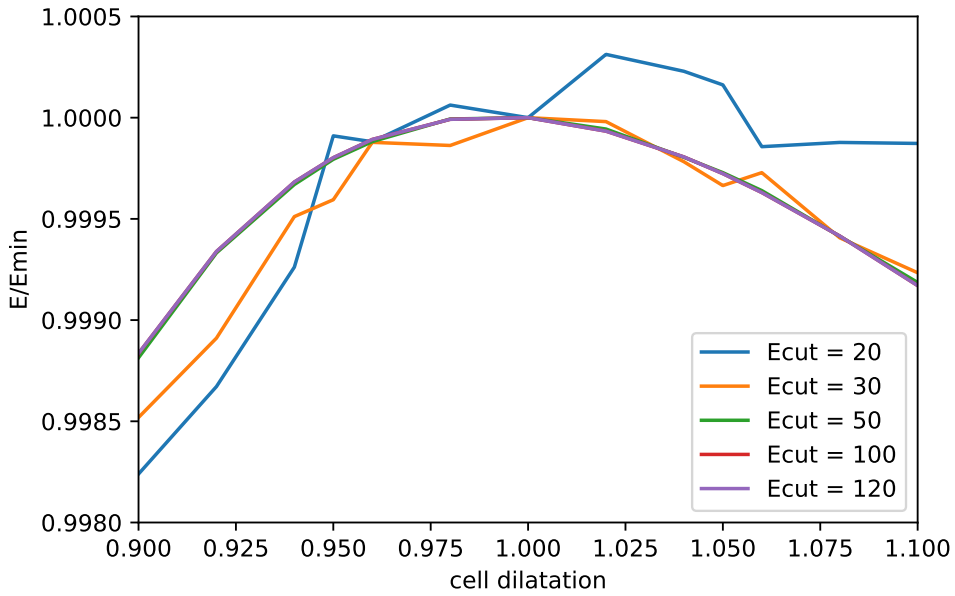

Figure A.1: Convergence respect to the pseudopotential energy cut applied

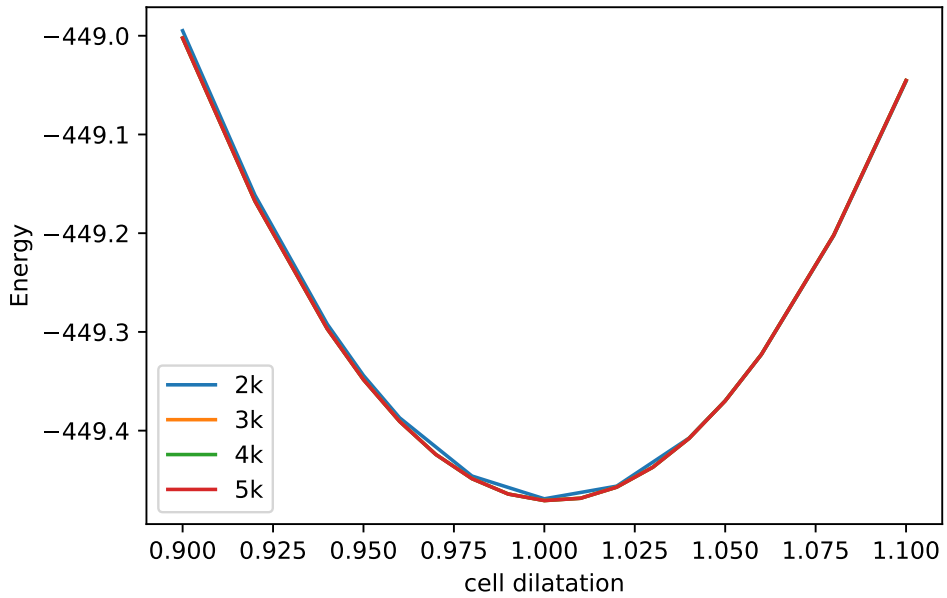

Figure A.2: Convergence respect to the different number of k-points used

Appendix B

Experimental configuration for sputtering deposition

Deposition of our samples required a close distance between sample and target of about 5 cm and a temperature of the substrate greater than 400 °C.
The available apparatus was indeed able to reach temperatures above 400 °C but was designed without the possibility to reach such a short distance so we designed a support that gave us the possibility to place the samples nearer the target while still conducting heat with the minimum dissipation.
Another constraint on the sample holder was placed by the weight limit because the structure wasn't designed to held a great load. The final prototype we crafted has a weight of around 100 g, is made out of copper and by a simple simulation, when the system thermalize, should held a temperature near 450 °C on the tip. In this appendix photo of the final configuration can be appreciated.

Choice of the target for the deposition was pretty much obliged. Fe:$LiNbO_3$ target commercially available were too thin to be used and the only one we tried shattered after a single utilize leading to a sample contamination. The problem was worked around by using a lithium niobate single crystal target adding on top of the surface some pieces of iron covering an area near the 1 % value.

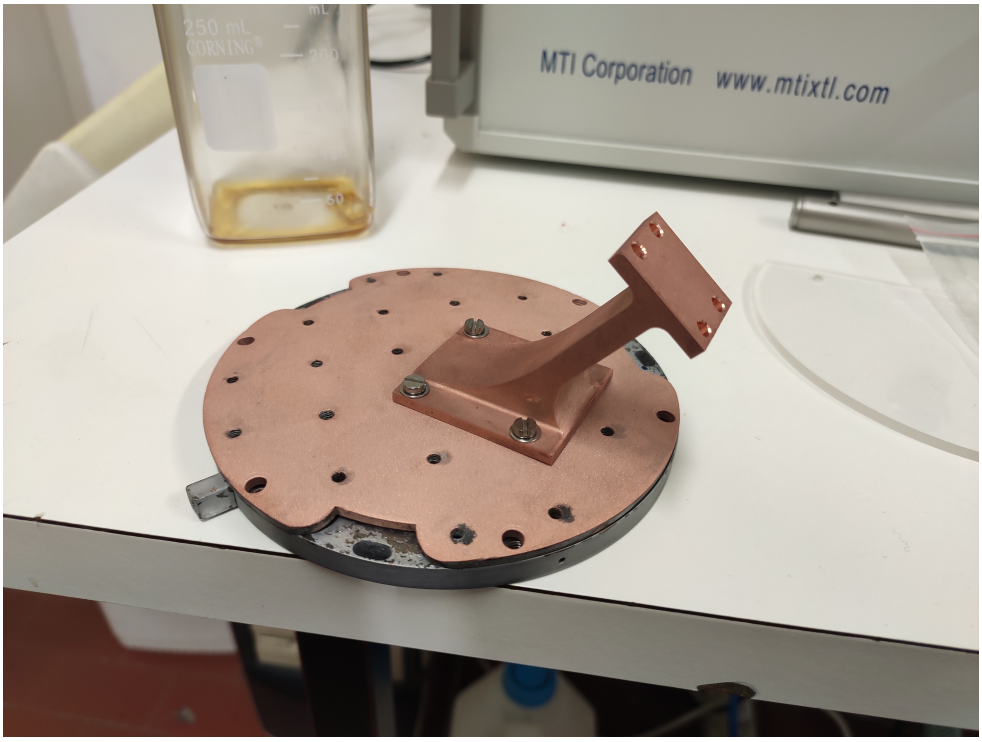

Figure B.1: Modified sample holder

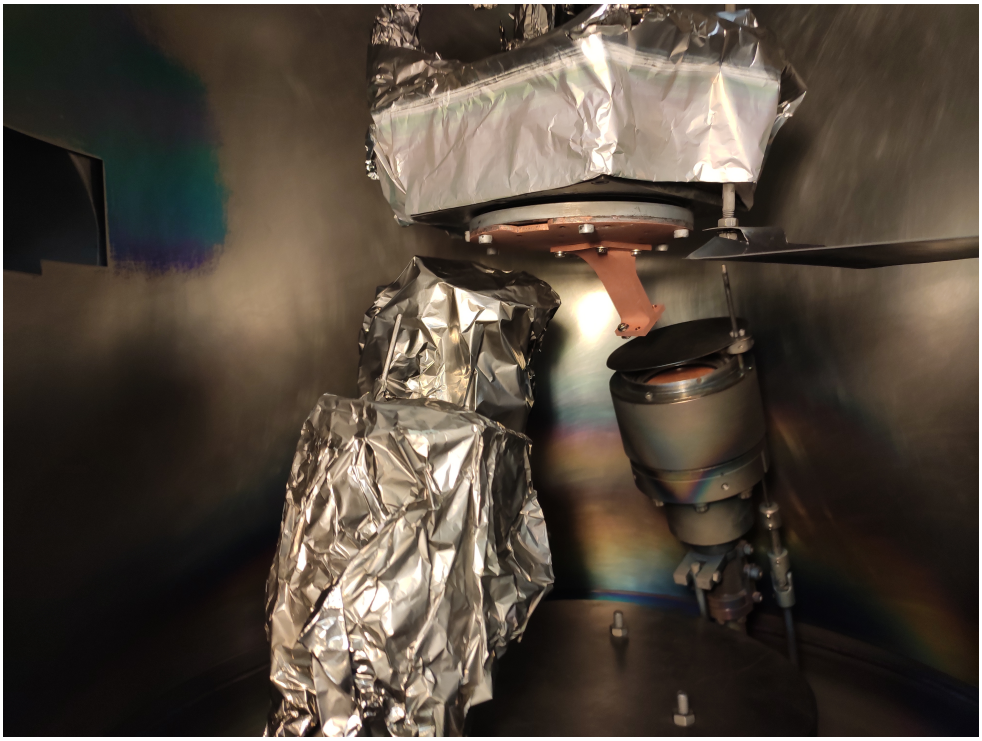

Figure B.2: Sputtering chamber final configuration

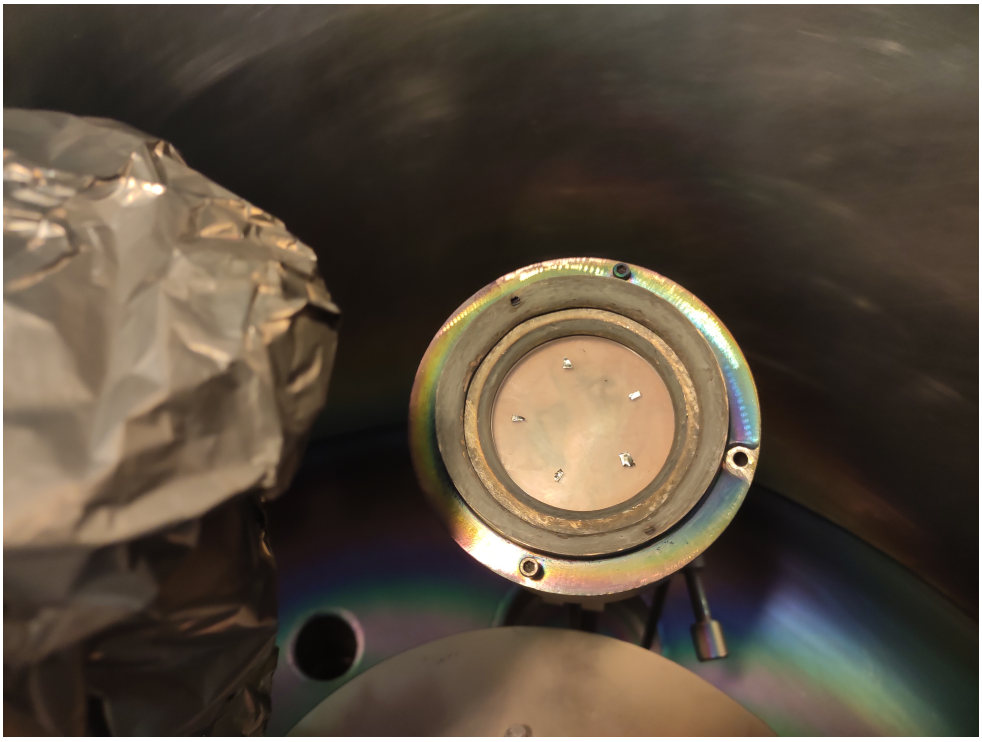

Figure B.3: $LiNbO_3$ target with iron added on the surface to reach near 1 % doping level

Appendix C

Transfer matrix method for optical multilayers

Let's consider the problem of a monochromatic wave with wave length λ propagating through a multilayered medium: a stack of materials with refractive index n_i and thickness d_i; an example of such a system is shown in Figure C.1
The waves that encounter interfaces between materials with different refractive indices will split in a transmitted and a reflected component, according to the Fresnel's laws. In general, the wave can undergo multiple reflections inside the material and, if the coherence length of the light is longer than the thickness of the different layers, it can end up with performing interference with itself, in a Fabry-Perot like fashion.
Computing the amplitude of a wave that undergoes such a process can be quite complicated as soon as the number of reflections start to grow. In the case of a single layer, neglecting multiple interference, one can still derive an analytical expression by summing up the intensities of the multiply- reflected beam. The final expression can be evaluated analytically by means of the geometrical series expression. However for already 2 layers this direct summation approach becomes much more complex. The transfer matrix method [14] is a simple technique that allow us to solve such a problem in a simple and elegant manner.
The starting point of the method is to assume that in a given slab the optical field is defined by two forward and backward propagating plane-wave beams with complex amplitudes $E_F(x_i)$ and $E_B(x_i)$. The relations between the electric field before and after an interface or while propagating through a media are found to be linear. So, the idea is that the net effect of any slab-like optical element, complicated it may be, can always be accounted for by a transfer matrix that relates the components of the electric field before and after the element itself. The equation we want to write will assume the form:

$$\begin{pmatrix} E_F(x_i) \\ E_B(x_i) \end{pmatrix} = \begin{bmatrix} A & B \\ C & D \end{bmatrix} \begin{pmatrix} E_F(x_f) \\ E_B(x_f) \end{pmatrix} = \boldsymbol{T}_{if} \begin{pmatrix} E_F(x_f) \\ E_B(x_f) \end{pmatrix} \tag{C.1}$$

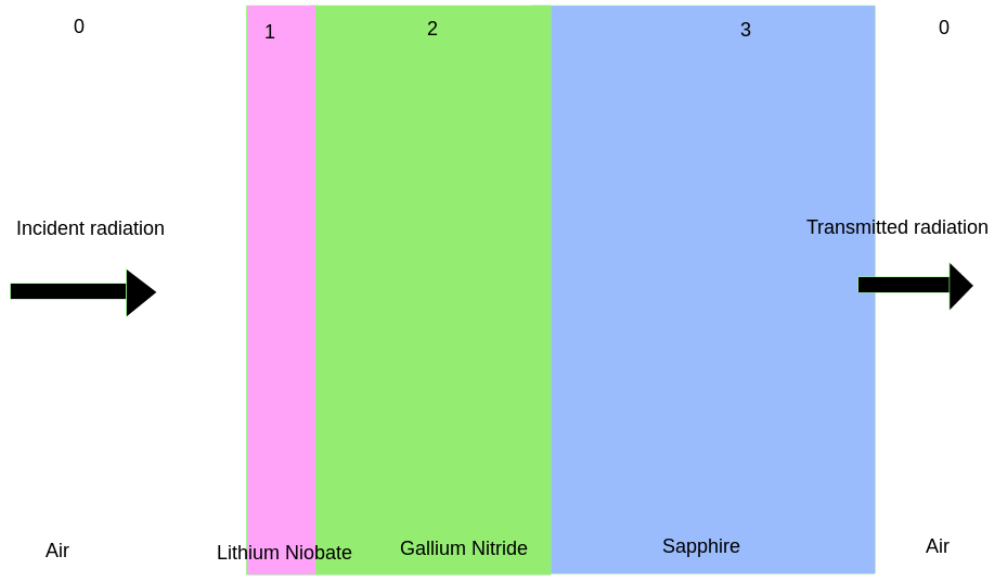

Figure C.1: Multilayered structure

where we can write the waves as $E(\vec{x}) = E_0 e^{i(\vec{k}\vec{x}-\omega t)}$ and the subscription F signals a forward propagation while the subscription B a backward one.
Let's start by considering a wave that moves trough a medium with thickness d and refractive index n at an angle θ from the surface normal. Since no interface is present, the reflected component must be zero so we can write:

$$\begin{pmatrix} E_F(x_i) \\ E_B(x_i) \end{pmatrix} = \begin{pmatrix} E_F(x_i) \\ 0 \end{pmatrix} = \begin{bmatrix} A & B \\ C & D \end{bmatrix} \begin{pmatrix} E_F(x_f) \\ E_B(x_f) \end{pmatrix} = \begin{bmatrix} A & B \\ C & D \end{bmatrix} \begin{pmatrix} E_F(x_f) \\ 0 \end{pmatrix} \tag{C.2}$$

To satisfy this relation we must put $C = B = 0$. If we work by neglecting the absorption, an assumption usually justified by the small thickness for which this approach is usually taken, the field amplitudes remains constant during the propagation and the net effect is a change to the wave phase of about $\Phi = \frac{2\pi}{\lambda} nd\cos\theta$. Our matrix for a wave through such a medium becomes:

$$T_i = \begin{bmatrix} e^{i\Phi} & 0 \\ 0 & e^{-i\Phi} \end{bmatrix} \tag{C.3}$$

In the case of a wave that encounters a surface between two materials with refractive index n_i and n_j the Fresnel coefficients r_{ij} and t_{ij} predict the amplitudes of the reflected and the transmitted waves. From basic knowledge of optical physics we can thus write:

$$E_F(x^+) = t_{ij} E_F(x^-) + r_{ji} E_B(x^+) \tag{C.4}$$
$$E_B(x^-) = r_{ij} E_F(x^-) + t_{ji} E_B(x^+) \tag{C.5}$$

and our matrix can be written as:

$$T_{ij} = \begin{bmatrix} \frac{1}{t_{ij}} & -\frac{r_{ji}}{t_{ij}} \\ \frac{r_{ij}}{t_{ij}} & t_{ji} - \frac{r_{ij}}{t_{ij}} r_{ji} \end{bmatrix} = \frac{1}{t_{ij}} \begin{bmatrix} 1 & r_{ij} \\ r_{ij} & 1 \end{bmatrix} \tag{C.6}$$

where we used the symmetry properties of the Fresnel coefficients $r_{ji} = -r_{ij}$ and $t_{ij}t_{ji} - r_{ij}r_{ji} = 1$ to simplify the expression.
The expressions we have found can now be put all together to build the general transfer matrix of a multilayered structure, so we can write our final matrix for a single layer:

$$\boldsymbol{T}_{i,j} = T_{ij}T_j \tag{C.7}$$

and since the wave that exit a material becomes naturally the wave that enter the next one:

$$\begin{pmatrix} E_F(x_{i_0}) \\ E_B(x_{i_0}) \end{pmatrix} = \boldsymbol{T}_{0,1} \begin{pmatrix} E_F(x_{f_1}) \\ E_B(x_{f_1}) \end{pmatrix} = \boldsymbol{T}_{0,1}\boldsymbol{T}_{1,2} \begin{pmatrix} E_F(x_{f_2}) \\ E_B(x_{f_2}) \end{pmatrix} = ... \tag{C.8}$$

$$\tag{C.9}$$

and our final transfer matrix simply becomes:

$$\boldsymbol{T}_{0,N} = \left(\prod_{i=1}^{N} \boldsymbol{T}_{i-1,i} \right) T_{N,0} \tag{C.10}$$

where the term $T_{N,0}$ is present because in general we are interested in the field that exit from our multilayered material.

Bibliography

[1] William Shockley and Hans J. Queisser (March 1961). "Detailed Balance Limit of Efficiency of p-n Junction Solar Cells" (PDF). Journal of Applied Physics. 32 (3): 510–519. Bibcode:1961JAP....32..510S. doi:10.1063/1.1736034

[2] S.Y. Yang; J. Seidel; S.J. Byrnes; P. Shafer; C.-H. Yang; M.D. Rossell; et al. (2010). "Above-bandgap voltages from ferroelectric photovoltaic devices" (PDF). Nature Nanotechnology. 5 (2): 143–7. Bibcode:2010NatNa...5..143Y. doi:10.1038/nnano.2009.451.

[3] V.M. Fridkin (2001). "Bulk photovoltaic effect in noncentrosymmetric crystals". Crystallography Reports. 46 (4): 654–658. Bibcode:2001CryRp..46..654F. doi:10.1134/1.1387133.

[4] Qian W. , Skowronski M., Rohrer G.R.Structural defects and their relationship to nucleation of GaN thin films. in III-Nitride, SiC, and Diamond Materials for Electronic Devices. Eds. Gaskill D.K, Brandt C.D. and Nemanich R.J., Material Research Society Symposium Proceedings, Pittsburgh, PA. 423 (1996), 475-486.

[5] LiNbO 3 thin film growth on (0001)-GaN Peter J. Hansen, Yutaka Terao, Yuan Wu, Robert A. York, Umesh K. Mishra, and J. S. Speck. Journal of Vacuum Science & Technology B 23, 162 (2005); doi: 10.1116/1.1850106

[6] A. M. Glass, D. von der Linde, and T. J. Negran, "High voltage bulk photovoltaic effect and the photorefractive process in LiNbO 3 ," Applied Physics Letters 25(4), pp. 233–235, 1974.

[7] P. Giannozzi, S. Baroni, N. Bonini, M. Calandra, R. Car, C. Cavazzoni, D. Ceresoli, G. L. Chiarotti, M. Cococcioni, I. Dabo, A. Dal Corso, S. Fabris, G. Fratesi, S. de Gironcoli, R. Gebauer, U. Gerstmann, C. Gougoussis, A. Kokalj, M. Lazzeri, L. Martin-Samos, N. Marzari, F. Mauri, R. Mazzarello, S. Paolini, A. Pasquarello, L. Paulatto, C. Sbraccia, S. Scandolo, G. Sclauzero, A. P. Seitsonen, A. Smogunov, P. Umari, R. M. Wentzcovitch, J.Phys.:Condens.Matter 21, 395502 (2009) http://dx.doi.org/10.1088/0953-8984/21/39/395502

[8] K. Nassau, H.J. Levinstein, G.M. Loiacono: J. Chem. Phys.Solids 27, 983-988 (1966)

[9] K. NASSAU, H. J. LEVINSTEIN, G. M. LOIACONO. Ferroelectric lithium niobate. 2. Preparation of single domain crystals. J. of Phys. Chem. Solids, 27, pp. 989-996, 1966.

[10] S. C. ABRAHAMS, J. M. REDDY, J. L. BERNSTEIN. Ferroelectric lithium niobate. 3. Single crystal X-ray diffraction study at 24 °C. J. of Phys. Chem. Solids, 27, pp. 997-1012, 1966.

[11] S. C. ABRAHAMS, W. C. HAMILTON, J. M. REDDY. Ferroelectric lithium niobate. 4. Single crystal neutron diffraction study at 24 °C. J. of Phys. Chem. Solids, 27, pp. 1013-1018, 1966.

[12] S. C. ABRAHAMS, H. J. LEVINSTEIN, J. M. REDDY. Ferroelectric lithium niobate. 5. Polycrystal X-ray diffraction study between 24 °C and 1200 °C. J. of Phys. Chem. Solids, 27, pp. 1019-1026, 1966.

[13] B. T. MATTHIAS, J. P. REMEIKA. Ferroelectricity in the Ilmenite Structure. Phys. Rev., 76, pp. 1886-1887, 1949.

[14] F. Abelès, Le Journal de Physique et le Radium, "La théorie générale des couches minces", 11, 307–310 (1950).

[15] Maria Vittoria Ciampolillo, Annamaria Zaltron, Marco Bazzan, Nicola Argiolas, and Cinzia Sada, "Quantification of Iron (Fe) in Lithium Niobate by Optical Absorption," Appl. Spectrosc. 65, 216-220 (2011)

[16] Lithium Niobate: Summary of Physical Properties and Crystal Structure R. S. Weis and T. K. Gaylord

[17] A. S. Barker Jr. and M. Ilegems. Infrared lattice vibrations and free-electron dispersion in GaN. Phys. Rev. B 7, 743-750 (1973)

[18] D. E. Zelmon, D. L. Small, and D. Jundt. Infrared corrected Sellmeier coefficients for congruently grown lithium niobate and 5 mol.% magnesium oxide-doped lithium niobate, J. Opt. Soc. Am. B 14, 3319-3322 (1997)

[19] M. J. Dodge, "Refractive Index" in Handbook of Laser Science and Technology, Volume IV, Optical Materials: Part 2, CRC Press, Boca Raton, 1986, p. 30

[20] Hubbard, J. (1963). "Electron Correlations in Narrow Energy Bands". Proceedings of the Royal Society of London. 276 (1365): 238–257. Bibcode:1963RSPSA.276..238H. doi:10.1098/rspa.1963.0204

[21] Measurement of bulk photovoltaic and photorefractive characteristics of iron doped LiNbO3 Journal of Applied Physics 54, 3012 (1983); https://doi.org/10.1063/1.332504

[22] A. Savage: J. Appl. Phys. 37, 3071-3072 (1966)

[23] Laura Vittadello, Marco Bazzan, Anush Danielyan, Edvard Kokanyan, Laurent Guilbert and Michel Aillerie 'A polaron approach to photorefractivity in Fe : LiNbO3' 2018 J. Phys. Commun. 2 125003; https://doi.org/10.1088/2399-6528/aaf3ec

[24] Wöhlecke, M., Corradi, G., Betzler, K. Appl. Phys. B (1996) 63: 323. https://doi.org/10.1007/BF01828734

[25] A. Ashkin, G. D. Boyd, J. M. Dziedzic, R. G. Smith, A. A. Ballman, J. J. Levinstein, and K. Nassau Appl. Phys. Lett. 9, 72 (1966); https://doi.org/10.1063/1.1754607

[26] J.F. Nye: Physical Properties of Crystals (Oxford U. Press, Oxford 1957)p. 115

[27] LiNbO3 films: Potential application, synthesis techniques, structure, properties. December 2017 Inorganic Materials 53(13):1361-1377 DOI: 10.1134/S0020168517130015

[28] Vook R W 1984 Nucleation and growth of thin films Opt. Eng. 23 343–9

[29] He J and Ye Z 2003 Highly C-axis oriented LiNbO 3 thin film on amorphous SiO 2 buffer layer and its growth mechanism Chin. Sci. Bull. 48 2290

[30] Park S-K, Baek M-S, Bae S-C, Kim K-W, Kwun S-Y, Kim Y-J and Kim J-H 1999 012) Preferred orientation of LiNbO 3 thin films by RF-magnetron sputtering Jpn. J. Appl. Phys.38 4167–71

[31] Hewig G M, Jain K, Sequeda F O, Tom R and Wang P-W 1982 R.F. Sputtering of LiNbO 3 thin films Thin Solid Films 88 67–74

[32] Shandilya S, Tomar M and Gupta V 2012 Deposition of stress free c-axis oriented LiNbO 3 thin film grown on (002) ZnO coated Si substrate J. Appl. Phys. 111 10–6

[33] A.W. Warner, M. Onoe, G.A. Coquin: J. Acoust. Soc. Am. 42, 1223-1231 (1967)

[34] R.T. Smith, F.S. Welsh: J. Appl. Phys. 42, 2219-2230 (1971)

[35] T. Yamada, N. Niizeki, H. Toyoda: Jpn. J. Appl. Phys. 6, 151-155 (1967)

[36] E.H. Turner: Appl. Phys. Lett. 8, 303-304 (1966)

[37] EM. Turner: J. Opt. Soc. Am. 56, 1426 (1966)

[38] PHYSICAL REVIEW B, VOLUME 65, 214302 First-principles study of the dielectric and dynamical properties of lithium niobate M. Veithen and Ph. Ghosez

[39] H. Boysen and F. Altorfer, Acta Crystallogr., Sect. B: Struct. Sci. B50, 405 1994.

[40] Park S K, Baek M S, Bae S C, Kwun S Y, Kim K T and Kim K W 1999 Properties of LiNbO 3 thin film prepared from ceramic Li-Nb-K-O target Solid State Commun. 111 347–52

[41] Rost T A, Lin H, Rabson T A, Baumann R C and Callahan D L 1992 Deposition and analysis of lithium niobate and other lithium niobium oxides by rf magnetron sputtering J. Appl. Phys. 72 4336–43

[42] Bornand V and Papet P 2005 LiNbO 3 -based ferroelectric heterostructures J. Phys. IV 126 89–92

[43] Ogale S B, Nawathey-Dikshit R, Dikshit S J and Kanetkar S M 1992 Pulsed laser deposition of stoichiometric LiNbO 3 thin films by using O 2 and Ar gas mixtures as ambients J. Appl. Phys. 71 5718

[44] N. Iyi, K. Kitamura, F. Izumi, J.K. Yamamoto, T. Hayashi, H. Asano, S. Kimura, J. Solid State Chem. 101, 340 (1992)

[45] G.G. DeLeo, J.L. Dobson, M.F. Masters, L.H. Bonjack, Phys. Rev. B 37, 8394 (1988)

[46] P. Lerner, C. Legras, J.P. Dumas, J. Cryst. Growth 3, 231 (1968)

[47] A.P. Wilkinson, A.K. Cheetham, R.H. Jarman, J. Appl. Phys. 74, 3080 (1993)

[48] Intrinsic LiNbO3 point defects from hybrid density functional calculations Yanlu Li, W. G. Schmidt, and S. Sanna Phys. Rev. B 89, 094111 DOI: 10.1103/PhysRevB.89.094111

[49] Lattice constants of K-and Mg-doped LiNbO3. Comparison with nonstoichiometric lithium niobate G. Malovichko, O. Cerclier, J. Estienne, V. Grachev, E. Kokanyan, and C. Boulesteix J. Phys. Chem. Solids 56, no. 9 (1995): 1285-1289 DOI: 10.1016/0022-3697(95)00058-5

[50] S. Rühle (2016). "Tabulated values of the Shockley–Queisser limit for single junction solar cells". Solar Energy. 130: 139–147. Bibcode:2016SoEn..130..139R. doi:10.1016/j.solener.2016.02.015

[51] Bulk photovoltaic effect of LiNbO3:Fe and its small-polaron-based microscopic interpretation O. F. Schirmer, M. Imlau, and C. Merschjann Phys. Rev. B 83, 165106

[52] V. Fradkin and R. Magomadov, "Anomalous photovoltaic effect in LiNbO 3 : Fe in polarized light," JETP Letters 30, pp. 686–688, 1979.

[53] First-principles study of microscopic properties of the Nb antisite in LiNbO3: Comparison to phenomenological polaron theoryH. H. Nahm and C. H. Park Phys. Rev. B 78, 184108

[54] Polaronic deformation at the Fe2+/3+ impurity site in Fe:LiNbO3 crystals A. Sanson, A. Zaltron, N. Argiolas, C. Sada, M. Bazzan, W. G. Schmidt, and S. Sanna Phys. Rev. B 91, 094109

Acknowledgment